Aspects of Electron Dynamics in Atoms Exposed to Single Cycle Electromagnetic Pulses

Michaela Chovancová

Thesis for the Degree of Philosophiae Doctor (PhD)
University of Bergen, Norway
2018

UNIVERSITY OF BERGEN

Aspects of Electron Dynamics in Atoms Exposed to Single Cycle Electromagnetic Pulses

Michaela Chovancová

Thesis for the Degree of Philosophiae Doctor (PhD)
at the University of Bergen

2018

Date of defence: 29.06.2018

Year: 2018

Title: Aspects of Electron Dynamics in Atoms Exposed to Single Cycle Electromagnetic Pulses

Name: Michaela Chovancová

Print: Skipnes Kommunikasjon / University of Bergen

Dissertation for the degree of Philosophiae Doctor (PhD)

Aspects of Electron Dynamics in Atoms Exposed to Single Cycle Electromagnetic Pulses

Michaela Chovancová

Department of Physics and Technology
Februar 2018

Abstract

This thesis covers the topic in atomic physics: Interaction of a strong external field with Rydberg hydrogen atom. In three scientific publications, we have targeted physical processes such as the field ionization in the strong terahertz field, back-scattering in the Coulomb field and spatial transport of electrons.
First two of them deal with the study of the ionization of the Rydberg atoms in the terahertz field. Rydberg atoms are highly excited stabilized states with very big dipole moments which makes them very sensitive to the external field. As external field we use THz radiation, submillimeter radiation in the range of 100 μm - 1 mm, which generators are in the state-of-the-art development. Specifically, we treat with linearly polarized single-cycle pulses with high intensity and picosecond duration. High intensity and low frequency brings us to the strong field, where the field is so strong, that Coulomb potential may be deformed and field ionization is possible.

Driving linearly polarized single-cycle pulse is only bidirectional, indeed the electron is driven mostly to the one direction by the field in the first half of the cycle and to the opposite direction in the second half. Affirmation is given by the observing of the probability density during the field propagation.
When some pulse asymmetry is included, then it involves new phenomena, which we have observed at different energy level of initial Rydberg states. While 15-d state may be ionized already in the first half of the pulse, where the sinus pulse has the opposite direction to the second half, lower energy states (6-d and 9-d) are ionized at the second half of the pulse with a higher peak intensity, at the opposite direction. Therefore, 15d electron has lower emission energy compare to lower lying Rydberg states.

We have numerically simulated the experiment published in April 2014 by Li and Sha (University of Virginia), where sodium d−Rydberg atoms have been ionized by single-cycle pulse with the duration 10-100 longer than electron Rydberg period and the ionization probability with increasing field strength has been measured. Curves in our simulation grow sigmoidally with the ionization scaling law n^{-3} for the field strength. This field strength scaling is inversely proportional to the binding energy of electrons in an atom and is valid for all of the probabilities, since all scaled probability curves meet at the same place on a plot. Explanation of this scaling law and mechanism behind is the main target of this thesis.
Ionization of bounded electrons by strong laser pulses occurs most frequently as over the barrier ionization, tunneling or multiphoton ionization.
By 3D analysis we concluded that the ionization takes the place mostly during the period around the field maxima. We suppose that the ionization is caused partly by the tunneling ionization for the field strength scaled as n^{-3} and partly as the over the barrier ionization scaled with the field strength as n^{-4}.
Angular distribution confirms that the electron density is located mostly in the direction of the field polarization. Backscattering shows that the part of the wavefunction is scattered back to the nucleus. The third paper comes with the spatial transport of an electron, when an electron is driven by the short strong external pulse(s). To observe this phenomena, the laser pulse frequency and the field intensity must be high enough, so that we can neglect the effect of the

Coulomb potential. Then wavefunction is translated almost without any distortion to a well defined distance from the origin. This distance depends just on the set up laser intensity and the frequency.

In quantum mechanics, wavefunction is propagated on the grid by the split-step operator and two-step Euler method. Classical simulations are calculated by the classical Monte Carlo method (CTMC). In this case, the initial state is modelled as the statistical microcanonical ensemble with set up boundary conditions . The classical differential equations are numerically solved by Euler method and Runge-Kutta method.

Acknowledgement

I want to thank to the whole department for giving me the opportunity to study this doctoral programme. I have been the part of the Optic and Atomic Physics group, where the atmosphere is friendly and supportive.
First of all, I want to thank my supervisor Prof. Jan Petter Hansen for all his work, friendly support and patience with me. I want to also thank to my co-supervisor Prof. Em. Ladislav Kocbach for discussions and suggestions to my work, to Dr. Hicham Agueny, the postdoc. in the Atomic Physics group at UiB, who has been developing code for the paper II. He is also the corresponding author of the paper II. I thank also to Jørgen Rørstad for his valuable master thesis and for all his help with CTMC computations.
My special thanks belongs to MSc. Jakub Višňák for his comments to my thesis and my family for their support.
I feel very grateful for having the opportunity to travel inside Norway and also to other countries for conferences and summer schools.

Contents

Chapter 1

Introduction

A discrete world consisting of the smallest indivisible particles called atoms was first proposed by Democritus in the ancient Greece. After a long period, in the end of the 19th century, sir Joseph Thompson discovered the first subatomic particle, the electron, in a beam of cathode rays in vacuum tube [1]. By electron deflection in electric and magnetic fields he was able to measure the ratio of the charge to the mass of the electron. He found that electrons are order of thousand times lighter than hydrogen atoms [2]. Soon after, in 1911, Rutherford discovered a localised positive field in the middle of an atom by scattering of alpha particles on the golden foil [3]. These two experiments established an atom, neutral as a whole, consisting of a small dense positively charged nucleus with negatively charged electrons around.

The theoretical basis for quantum mechanics is commonly seen to have started with the explanation of the emission spectrum of a *black body* at fixed temperature, T [1]. According to the classical theory, we cannot describe the black body radiation energy density function $\rho(T,\nu)d\nu$ in the short-wavelength limit, because it produces infinite radiation intensity. The German physicist Max Planck was able to fit experimental data of the black body radiation curve with a new distribution function. The function, now called the Planck curve, depended on a new constant $h \sim 6.6310^{-34}$ Js [4], later called Planck's constant. Using this, Einstein was in 1905 able to explain the photoelectric effect [5]. He assumed that light is a stream of particles, light quanta, each with energy $E = h\nu$. The word *photon* for a quantum of light was for the 1'st time used by Gilbert N. Lewis 21 years after Einstein's explanation.

In 1913 Niels Bohr explained the emission spectra of hydrogen given by a completely new model. [6]. He assumed that angular momentum ,l, in certain stable states are quantised in integer numbers of $\hbar = h/2\pi$, ie. $l = n\hbar$. When using classical mechanics and this assumption, the energy levels of discrete states appear as

$$E = -\frac{Ry}{n^2}, \tag{1.1}$$

where the Rydberg constant is $Ry \sim 13.6$ eV. The notion of stable trajectories remained a contradiction to classical electromagnetic theory, where all accelerating particles radiates energy.

A wave-particle duality valid for any particle on the small scale were proposed by Louis de Broglie in 1924 in his dissertation, where he quantifies the (non-relativistic) particle wavelength as $\lambda = h/p$, where p is the particle momentum [7]. To defend the equation in his thesis,

[1] A black body is an idealized body definied by its capability to emit and absorb electromagnetic radiation at any wavelength

de Broglie suggested electron scattering and diffraction experiments as an experimental test. This experiment was carried out in 1927 by Davisson and Germer [8]. The same year, G. P. Thompson and A. Reid observed interference pattern of electrons, by passing a beam of electrons through a thin metal film [9]. Interference pattern from a single-electron double slit experiment was obtained by Merli, Missiroli and Pozzi as late as in 1976 [10].

A grand challenge of physics became the quest for an equation valid on the atomic and subatomic level and being an equivalent to Newton's equation on the macroscopic scale. The problem was solved by Erwin Schrödinger in 1926 as he has assigned to a particle a complex wave function, $\psi(r,t)$ which satisfy a second-order time dependent or time independent linear partial differential equation [11]. The equations, today known as the Schrödinger Equation and the time-dependent Schrödinger Equation, became a cornerstone of modern physics. The time dependent equation is written on his gravestone in Alpbach, Austria. The interpretation of the wavefunction has been an ongoing branch of quantum physics and philosophy ever since its invention. The most accepted one originates from Max Born [12, 13]. His statistical interpretation defines $|\psi(r,t)|^2 d^3r$ as the the probability that a particle is located around a region d^3r at a time t.

We can experience application of quantum physics, quantum technologies, everywhere around us today. Atomic clocks define a second very accurately in terms of two energy states in the caesium atom. Coherent light from lasers is possible due to the population inversion of quantum states by stimulated emission. Transistors, semi-conductors and diodes in electronic devices are designed with the knowledge of quantum energy states and quantum phenomena such as tunnelling and the quantum Hall effect [14]. Based on the quantum tunneling we can detect magnetic and electric field very accurately, up to 10^{-18} scale in respective SI units. In fact, material science, chemistry, medicine and industry have all been developed based on the development of quantum physics. Nowadays, experiments shedding light on the fundamentals of quantum mechanics continue. For example, less than two decades ago, attosecond pulses opened the way for researchers to follow electronic motion inside atoms and molecules [15, 16]. As it has become possible to make one layer diffraction slits atomic size, we can catch high-resolution images of complex organic molecules [17, 18]. Research on control of coherent quantum state [19] is very promising for applications in spintronics and quantum information [20, 21]. These are only few examples from a jungle of ongoing current research. The present thesis, and the results, connects to all of the examples above. We study electron propagation inside a single atom and discuss conditions for quantum control and potential applications for imaging.

This thesis consists of a general introduction to methods and theories of which the scientific results in the form of three published papers and developed programs have been based. It follows this introduction as four chapters ending with conclusion and outlook. For generality we use SI units with a few exceptions in this first section of Chapter 2. In the remaining part of the thesis and in the scientific papers we apply more conveniently atomic units. The connection between the two sets of units is defined in appendix. A second appendix details the development of a scattering formula applied in paper II.

Chapter 2

Atoms and their interaction with electromagnetic fields: Semiclassical theory

At the most fundamental level, charged particles and their time dependent interaction with strong electromagnetic fields would be described by quantum field theory. We are not aware of any such schemes being formulated and it would indeed in the end require a prohibitive amount computational resources. A less unrealistic treatment would be to consider atoms as composed non-relativistic particles interacting with a quantized photon field. This is a standard approach for atoms interacting with few photon fields. However, strong fields imply extremely large photon numbers, which without simplifications would fill the memory of any computer several times. And on the other hand, from the perspective of the field, the physical properties are hardly altered by a tiny interaction with a single atom. This suggests a semiclassical approximation where the atom is treated in quantum mechanical terms and interacts with a classical time dependent electromagnetic field. This approach has a long standing history in collision physics [22]. For electromagnetic fields it was formally derived by Briggs and Rost as late as in 2001 [23]. Thus, the photon field is described by Maxwell's equations and the interaction with matter takes place through the interaction part of the Hamiltonian. In the following sub-chapters this approach is described in detail.

2.1 Classical electromagnetic field

As early as in 1865 Maxwell had managed to unified general laws of the electromagnetic radiation into four equations [24]. In atomic physics it is particularly useful to introduce Maxwell equations in terms of the two mathematical quantities, a scalar potential (ϕ) and a vector potential ($\mathbf{A}$),

$$-\boldsymbol{\nabla}^2\phi + (\frac{1}{c^2}\frac{\partial^2\phi}{\partial t^2}) = \frac{\rho}{\varepsilon_0} \tag{2.1}$$

$$-\boldsymbol{\nabla}^2\mathbf{A} + \frac{1}{c^2}\frac{\partial^2\mathbf{A}}{\partial t^2} = \mu_0\mathbf{J}, \tag{2.2}$$

Here the speed of light is $c = 1/\sqrt{(\varepsilon_0\mu_0)}$ is ~ 137 a.u., the permeability of vacuum is ε_0 and the magnetic permitivity of vacuum is μ_0. The equations here are presented in the Lorenz

gauge, where $\nabla \cdot \mathbf{A} = -\partial\phi/(c\partial t)$. The electric and magnetic fields can be expressed by the potentials as

$$\mathbf{B}(\mathbf{r},t) = \nabla \times \mathbf{A}(\mathbf{r},t) \tag{2.3}$$

$$\mathbf{E}(\mathbf{r},t) = -\nabla\phi(\mathbf{r},t) - \frac{1}{c}\frac{d\mathbf{A}(\mathbf{r},t)}{dt} \tag{2.4}$$

The potential representation has four variables ϕ, A_x, A_y and A_z in contrast to 6 given by the electric and magnetic fields. This open for certain freedoms (gauge choices) in choosing the potentials to work with. In strong field physics, we can take $\phi = 0$, ie. no point charges, and $\nabla \cdot \mathbf{A} = 0$. The latter condition is called the "Coulomb gauge" but can be seen as a special case of the Lorenz gauge. The solution of Maxwell's equations in free space is then a set of plane waves of the form

$$\mathbf{A}(\mathbf{r},t) = A_0\hat{\varepsilon}\cos(\mathbf{k}\cdot\mathbf{r} - \omega t) \tag{2.5}$$

where ω is the frequency of the oscillation, $\mathbf{k}$ is the wave vector with the magnitude $k = \omega/c$, A_0 is the wave amplitude directed along the polarization unitary vector $\hat{\varepsilon}$. From Eq. (2.4) we obtain the electric field,

$$\mathbf{E}(\mathbf{r},t) = E_0\hat{\varepsilon}\sin(\mathbf{k}\cdot\mathbf{r} - \omega t) \tag{2.6}$$

with $E_0 = \omega A_0$. The magnetic field becomes perpendicular to the electric field,

$$\mathbf{B} = (\mathbf{k}\times\hat{\varepsilon})A_0\cos(\mathbf{k}\cdot\mathbf{r} - \omega t) \tag{2.7}$$

Comparing amplitudes of electric and magnetic field $E_0/B_0 = \frac{\omega}{|k|} = c$, we observe that the magnetic field strength is $1/c$ smaller than the electric field strength. Considering further, the wavelength of the external fields $\lambda = 2\pi c/\omega$, we realize that it is, for field frequencies normally well below unity, orders of magnitude larger than the size of atoms. This verifies the widely used dipole approximation where the spatial dependence of the vector field is ignored across the atom,

$$\mathbf{A}(\mathbf{r},t) \sim A_0\hat{\varepsilon}\cos(\omega t). \tag{2.8}$$

This result in a corresponding simplified approximate electromagnetic field as well

$$\mathbf{E}(\mathbf{r},t) \sim \omega E_0\hat{\varepsilon}\sin(\omega t) \tag{2.9}$$

and a vanishing magnetic field. Any constant phase shift may be added to this expression. This approximation is applied throughout the present work. Even if Rydberg atoms are large and extend up to hundreds of a.u., the angular frequencies are in the range from $10^{-5} - 10^{-3}$ a.u., giving $137/\omega$ is in the range $10^3 - 10^6$.

2.2 Schrödinger Equations of the Atom

In 1926 Schrödinger published wave-equations of a bound particle based on Hamiltonian $\hat{H}$, the operator of the system energy [11], acting on a new object, the wave-function. He introduced first the time-independent equation (TISE), which solutions are stationary states with discrete or a continuous set energy values. Later the same year, a time dependent equation were put forward

(TDSE) to describe quantum dynamics. These equations substitute Newton's mechanics on the sub-micrometer scale. For his discovery of "new productive forms of atomic theory" he received the Nobel Prize in Physics 1933 together with Paul Adrien Maurice Dirac. The same year Heisenberg received the Nobel Prize for 1932 for having, one year before Schrödinger, developed a separate operator based approach to quantum mechanics. In one of the six famous papers of Schrödinger in 1926 he demonstrates that Heisenbergs and his own formalism leads to completely identical results. The time-independent Schrödinger equation is an eigenvalue equation

$$\hat{H}\Psi(\mathbf{r}) = E\Psi(\mathbf{r}) \tag{2.10}$$

where $\hat{H} = \hat{p}^2/2 + V(\hat{r})$ is the quantized form of the classical Hamiltonian of the particle and E is the energy. The quantization rule is $\hat{p}_i = -\frac{\partial}{\partial x_i}$ and $\hat{x}_i = x_i$, and leads to the following three-dimensional Hamiltonian operator for a single electron

$$\hat{H} = -\frac{1}{2}\boldsymbol{\nabla}^2 + V(\mathbf{r}) \tag{2.11}$$

Here the first term represents the kinetic energy and the second term is the potential energy. There are a number of potential energy cases for which the TISE can be solved analytically, e.g., $V = 0$ (free particle), $V = 1/2\omega^2\mathbf{r}^2$ (harmonic oscillator) and $V = -1/\mathbf{r}$ (hydrogen atom). For arbitrary potentials, analytical solutions are not known. But the equation may in this case always be solved numerically. In case of atoms with many interacting electrons, there are no analytical solutions at all and even numerical solutions can become difficult to achieve.

The details of the solution for bound states of the hydrogen atom are now outlined as a short example of a solvable system. The Coulomb potential then suggest the use of spherical coordinates, where the position of an electron is given by the radius r, azimuthal angle ϕ and zenith angle θ. The scalar operator $\boldsymbol{\nabla}^2$ (2.11) takes the form

$$\boldsymbol{\nabla}^2 = \frac{1}{r^2}\frac{\partial}{\partial r}(r^2\frac{\partial}{\partial r}) + \frac{1}{r^2\sin\theta}\frac{\partial}{\partial\theta}(\sin\theta\frac{\partial}{\partial\theta}) + \frac{1}{r^2\sin^2\theta}\frac{\partial^2}{\partial\phi^2} \tag{2.12}$$

which can be shortened as

$$\boldsymbol{\nabla}^2 = \frac{1}{r^2}\frac{\partial}{\partial r}(r^2\frac{\partial}{\partial r}) - \frac{\hat{L}^2}{r^2} \tag{2.13}$$

with $\hat{\mathbf{L}}$ being the angular momentum operator. The TISE for a hydrogen like atom now takes the form

$$\left[-\frac{1}{2}(\frac{\partial^2}{\partial r^2} + \frac{2}{r}\frac{\partial}{\partial r} - \frac{1}{r^2}\hat{L}^2) - \frac{Z}{r}\right]\Psi(r,\theta,\phi) = E\Psi(r,\theta,\phi) \tag{2.14}$$

The solution $\Psi(r,\theta,\phi)$ can be separated in a radial part $R_{n,l}(r)$ and spherical harmonics eigenfunctions $Y_l^{m_l}(\theta,\phi)$. Three quantum numbers appear, n is principal quantum number, l is angular quantum number, m_l is the projection of angular quantum number on the arbitrary chosen z-axis,

$$\begin{aligned} n &\in 1, 2... \\ l &\in 0, 1...n-1 \\ m_l &\in -l...l \end{aligned} \tag{2.15}$$

Each set (n,l,m) defines a possible eigenstate with energy 1.1.

$$E_n = -\frac{1}{2n^2} \tag{2.16}$$

The eigenstate takes the form

$$\Psi_{n,l,m_l}(\mathbf{r},\theta,\phi) = R_{n,l}(r)Y_l^{m_l}(\theta,\phi) = R_{n,l}(r)Y_l^{m_l}(\theta)e^{(}im_l\phi) \tag{2.17}$$

The radial solution of the Schrödinger equation has a general form of a product of the normalized condition, power function, polynomial and exponential part,

$$R_{n,l}(r) = N_{n,l}r^l\tilde{P}_{n,l}(r)e^{(} - Zr/n) \tag{2.18}$$

where $N_{n,l}$ is the normalization constant and $P_{n,l}(r)$ is a polynomial in r. We note the exponential damping which sets the scale of the state n. The angular part has a general form

$$Y_l^{m_l} = A_{l,m_l}P_l^{m_l}(\cos(\theta))e^{im_l\phi} \tag{2.19}$$

where A_{l,m_l} is the norm of spherical harmonics functions, $P_l^{m_l}$ are associated Legendre polynomials. To each state at the hydrogen energy level with number n are assigned $n-1$ states with different angular momentum l. This is due the fact, that angular momentum l_z is quantized. Similarly, for given values of n and l, there are $(2l+1)$ states with $m_l = -l..,0,..l$, which are degenerated. The degree of degeneracy of the energy level E_n is therefore $\sum_{l=0}^{n-1}(2l+1) = n^2$, and this degeneracy is a trademark of the Coulomb potential only.

A common numerical approach for obtaining approximate solutions to the eigenstates is to take advantage of the expansion of the wavefunction in a known analytical basis of N eigenstates $[\phi_i(\mathbf{r})]$ which forms an orthonormal basis. Explicitly inserted in the TISE,

$$\sum_{i=0}^{N}\left[-\frac{1}{2}\nabla^2 + V(\mathbf{r})\right]c_i\phi_i(\mathbf{r}) = E\sum_{i=0}^{N}c_i\phi_i(\mathbf{r}) \tag{2.20}$$

To obtain the solution we multiply eq. (2.20) sequentially by all basis functions ϕ_j from the left and obtain an eigenvalue problem for the vector of expansion coefficients, $\mathbf{c} = (c_0, c_1 ... c_N)$

$$\mathbf{Hc} = E\mathbf{c} \tag{2.21}$$

Now $\mathbf{H}$ becomes a matrix with elements,

$$H_{i,j} = \int d^3r\phi_i^*(\mathbf{r})\left[-\frac{1}{2}\nabla^2 + V(\mathbf{r})\right]\phi_j(\mathbf{r}) \tag{2.22}$$

The integrals needs to be calculated in advance, and this particular operation depends heavily on the choice of basis functions. The number of basis functions necessary for convergence is also strongly sensitive to the type of basis functions. A vast number of algorithms and packages are available for diagonalization.

The time-dependent Schrödinger equation, TDSE, has the form

$$i\frac{\partial\psi(\mathbf{r},t)}{\partial t} = \hat{H}\psi(\mathbf{r},t) \tag{2.23}$$

When the Hamiltonian is independent of time, the solution of the TDSE is separable and reduces to the TISE for a time independent wavefunction $\psi(r)$. The time dependent solution becomes

$$\psi(\mathbf{r},t) = \psi(\mathbf{r})e^{-iEt} \tag{2.24}$$

where E is the separation constant which is associated with the energy. A time-dependent Hamiltonian often has a well known spectrum of states at the initial time, $t = 0$, $\psi_n(\mathbf{r},t = 0)$, where n can take a finite of infinite values. A common *ansatz* is then to express the time dependent wavefunction in terms of a linear time-dependent sum of the spectrum of states,

$$\psi(\mathbf{r},t) = \sum_{n=0}^{N} c_n(t)\psi_n(\mathbf{r}) \tag{2.25}$$

If the system initially is in the first state we have $c_n(t = 0) = \delta_{n,0}$. Further more, the amplitudes can be interpreted as the probability of the system to be in the state n at given time t. More formally, the solution of the TDSE can be written as

$$\psi_n(\mathbf{r},t) = \hat{U}(t_0,t)\psi_n(\mathbf{r},t_0) \tag{2.26}$$

where $\hat{U}$ is a unitary time-evolution operator and takes a form

$$\hat{U}(t_0,t) = e^{-i\int_{t_0}^{t}\hat{H}(t-t_0)dt} \tag{2.27}$$

We can derive the unitary operator from the TDSE

$$i\frac{\partial\hat{U}}{\partial t} = \hat{H}\hat{U} \tag{2.28}$$

The unitary operator is transitive

$$\hat{U}(t_1,t_2)\hat{U}(t_2,t_3) = \hat{U}(t_1,t_3) \tag{2.29}$$

$$\hat{U}(t_2,t_1) = \hat{U}^{-1}(t_1,t_2) = U^{\dagger}(t_1,t_2) \tag{2.30}$$

This implies that the norm of the state $\psi(r,t_1)$ is not changed during the time-propagation,

$$\frac{d}{dt}\int_{\mathbb{R}^3}\psi^*(\mathbf{r},t_1)\psi(\mathbf{r},t_1)dr = 0, \quad \forall t \tag{2.31}$$

If the Hamiltonian commute with itself at different times $[\hat{H}(t_0),\hat{H}(t)] = 0$ and we consider a small timestep $t - t_0 << 1$ an approximate expression of the time-evolution operator becomes,

$$\hat{U}(t_0,t) = e^{-i\hat{H}(t-t_0)} \tag{2.32}$$

This approximation is a useful starting point for numerical algorithms, as will be discussed in Chapter 4. In theory, space and basis are infinite, but in practice we need to work in the finite space and time. Thus, any numerical discretization involves at least some level of approximation (truncation error). In our case space grid is very large (10^5 a.u.) with the smooth absorbator on both edges, so that a wavefunction was kept mostly on the grid during the propagation. We assume the absorbed part of the wavefunction to be in continuum.

2.3 Interaction between atoms and electromagnetic fields

The interaction between the quantum mechanical atom and the predefined, time-dependent electromagnetic free ($\phi = 0$) field is now described in the dipole approximation through the Hamiltonian

$$\hat{H}^{VG} = \frac{1}{2}\left[\hat{\mathbf{p}} - \mathbf{A}\right]^2 + V((\hat{r}) = \hat{H}_0 + \underbrace{\mathbf{A}\cdot\hat{\mathbf{p}} + \frac{\mathbf{A}^2}{2}}_{\hat{H}_i} \tag{2.33}$$

The first term $\hat{H}_0$ describes the Hamiltonian of the atom while the second term describes the interaction of atom with the field. Within the dipole approximation, the last term with $\mathbf{A}^2$ is just a time-dependent phase, which can be removed from the numerical scheme by multiplying with a global phase factor

$$\psi^{VG}(\mathbf{r},t) \rightarrow \psi^{VG}(\mathbf{r},t)e^{(}\frac{-i}{2}\int_{t_0}^{t}\mathbf{A}^2(t')dt') \tag{2.34}$$

We arrive at the following expression for the TDSE

$$\left[\frac{\hat{\mathbf{p}}^2}{2} + V(r) - \mathbf{A}\cdot\hat{\mathbf{p}} - i\frac{\partial}{\partial t}\right]\psi^{VG}(\mathbf{r},t) = 0 \tag{2.35}$$

with the interaction term now reduced to $\hat{H}_i = \mathbf{A}\cdot\hat{\mathbf{p}}$. An alternative expression in terms of the electric field $\mathbf{E}$ is

$$\left[\frac{\hat{\mathbf{p}}^2}{2} + V(\hat{r}) - \mathbf{r}\cdot\mathbf{E} - i\frac{\partial}{\partial t}\right]\psi'^{LG}(\mathbf{r},t) = 0 \tag{2.36}$$

where the term in the parenthesis represents the Hamiltonian in the length gauge. We can transform the wavefunction from the velocity gauge to length gauge via

$$\psi^{LG}(\mathbf{r},t) = e^{-i\mathbf{r}\cdot\mathbf{A}(t)}\psi^{VG}(\mathbf{r},t) \tag{2.37}$$

which can be shown by inserting the latter expression in Eq. (2.33). An alternative expression in terms of the electromagnetic field itself is the moving Kramers-Henneberger frame (KH). We can transform the Hamiltonian as $\hat{H}^{KH} = \hat{T}^{-1}\hat{H}\hat{T}$ to a moving frame centered at $\boldsymbol{\alpha}(t)$ by

$$\hat{T} = e^{-i\boldsymbol{\alpha}(t)\cdot\hat{\mathbf{p}})} \tag{2.38}$$

where the translation (or displacement) vector $\boldsymbol{\alpha}(t) = -\int_{t_0}^{t}\mathbf{A}(t')dt'$. Thus, any eigenstate of the Hamiltonian, where $\boldsymbol{\alpha}(t) = 0$ transforms to frame with origin at $\boldsymbol{\alpha}(t)$ as,

$$\Psi_n^{KH}(\mathbf{r} - \boldsymbol{\alpha}(t),t) = e^{i\boldsymbol{\alpha}(t)\cdot\hat{\mathbf{p}})}\Psi_n^{VG}(\mathbf{r},t) \tag{2.39}$$

The time-dependent Schrödinger equation in the KH frame then becomes

$$\left[\frac{\hat{\mathbf{p}}^2}{2} + V\left[\mathbf{r} - \boldsymbol{\alpha}(t)\right] - i\frac{\partial}{\partial t}\right]\psi^{KH}(\mathbf{r} - \boldsymbol{\alpha}(t),t) = 0 \tag{2.40}$$

The displacement vector $\boldsymbol{\alpha}(t)$ describes the rest frame of a free classical particle in the oscillating field. In this frame the particle is exposed to the time-dependent nuclear potential $V(\mathbf{r} - \boldsymbol{\alpha}(t))$ which can cause transitions among states described in a a stationary frame.

In principle the number of alternative transformations of the Hamiltonian is infinite. The three representations here derived do however dominate applications for which the dipole approximations hold. None of them are supperior to other in the general case. The VG, in combination with expansions in terms of spherical harmonics, has shown to be most effective for strong pulse physics [28]. In certain cases, in particular when intra shell dynamics in Rydberg atoms are considered, the length gauge has certain advantages. The LG additionally has the convenient property that the kinetic and canonical momentum are equal while in VG the canonical momentum is $\mathbf{p}-\mathbf{A}(t)=\mathbf{p}-\dot{\boldsymbol{\alpha}}(t)$. Finally, in situations where the field is so strong that the entire wavefunction remains localized around the displacement paramter, the KH frame is advantageous.

We end this chapter with a short discussion of an applied single cycle pulse in the present work. It is inspired by an experiment published in 2014 by Li and Jones [26]. The electric z-polarized field $\mathbf{E}(t)=E(t)\mathbf{e}_z$, is given as,

$$E(t)=\begin{cases}-E_0\sin(\omega t), & \text{if } -T<t<0\\ -E_0\beta\sin(\beta\omega t), & \text{if } T/\beta>t>0\\ 0 & \text{otherwise}\end{cases} \tag{2.41}$$

where for the experimental pulse in [26] $\beta=1.5$ fits reasonable well the experimental features. The analytical form of the vector field is then

$$A(t)=\begin{cases}-\frac{E_0}{\omega}\cos(\omega t+1), & \text{if } -T<t<0\\ -\frac{E_0}{\omega}\beta\cos(\beta\omega t+1), & \text{if } T/\beta>t>0\\ 0 & \text{otherwise}\end{cases} \tag{2.42}$$

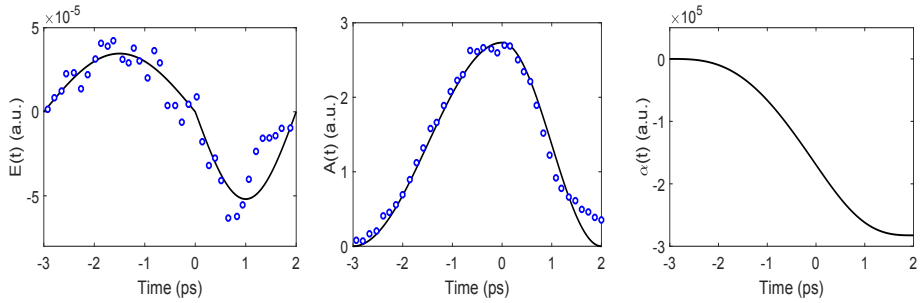

Figure 2.1: Time dependence of the the electric field strength $E(t)$ (lef) along the z-direction and the vector potential $A(t)$ (middle) for a single-cycle pulse. The black line represents the model pulse and the blue dots are experimental data [26]. The right panel shows the displacement $\alpha(t)$ eq. (2.43).

Finally the displacement becomes

$$\alpha(t)=\begin{cases}-\frac{E_0}{\omega}(t+T)-\frac{E_0}{\omega^2}\sin(\omega t), & \text{if } -T<t<0\\ -\frac{E_0}{\omega}(t+T)-\frac{E_0}{\beta\omega^2}\sin(\beta\omega t), & \text{if } T/\beta>t>0\,.\\ 0 & \text{otherwise}\end{cases}$$

The electric pulse is characterized by a positive first half cycle and a slightly shorter and more intense negative half cycle. When exposing this pulse shape to excited atoms it will, for sufficiently strong peak field parameter E_0, ionize a part or the entire atom. The electron is brought to the continuum and accelerated in along the negative z-direction. At some point the field turns and the positive acceleration brings the electron to a standstill or to a back-propagation towards the nucleus. Thus, the main part of the electron spectrum in this case is expected to scatter in the positive direction. Note the order of magnitude difference in pulse strength between the vector potential and the electric field. Correspondingly, the value of $\alpha(T/\beta)$ becomes very large. This poses a particular challenge for numerical simulations, to be described in Chapter 4.

Chapter 3

Atoms and their interaction with electromagnetic fields: CTMC

Even though the behaviour of electrons in atoms is governed by quantum mechanics, it can be useful to have a classical model to help understanding of ongoing processes. However, quantum mechanics is probabilistic in the nature. Therefore, by classical physics we cannot describe pure quantum phenomena like for example tunnelling or interference. Nevertheless we may set up a completely classical model where the electrons are propagated according to Newton's laws and investigate to which extent it reproduces the quantum calculations. This requires, of course, that the atom interact with the electromagnetic field solely through the Lorentz force.

A classical method used here is called the classical trajectory monte carlo (CTMC). This method uses a large ensemble of identical particles, a microcanonical distribution, which identifies possible states of a studied system by allowed number of particles N, volume ν and energy E_0. In fact, these three values N, ν, E_0 are initial conditions to the equations given by the classical mechanics. To simulate atomic states, the notion of electronic trajectories around nucleus with fixed energy $E_0 = -0.5/n^2$ is deployed. First we define a set of all possible positions and momenta pictured as radial microcanonical distributions, all these possible states are developed in time by the deterministic Newton's differential equations, which gives us initial trajectories around the nucleus and set of final positions and momenta for analysis after interacting with the electromagnetic field.

Monte Carlo methods were invented by Stanislaw Ulam, Nicholas Metropolis and von Neumann in the 1940's [29, 30]. Abrines and Percival described the CTMC method in the original article [31] with initial states based on microcanonical ensembles. The method was demonstrated in collisions between the ground state hydrogen and proton and the ionization and charge-transfer cross sections have been computed. As the method resulted in cross sections and electron spectra in relatively good agreement with experiments [31, 32], it became popular and further developed and extended. Reinhold and Falcón [33] simplified the microcanonical distribution to the form as described in this chapter.

Adding the quantum phases of the electron along a classical electron trajectory makes possible to even reconstruct the interference pattern of photoelectron emission spectra [35, 36] or diffraction patterns [37]. This approach is based on Feynman path integrals [38] and defines so called quantum-trajectory methods. The classical action,

$$S(r_1,t_1;r_0,t_0) = \int_{t_0}^{t_1} L(\mathbf{x}(t),\mathbf{v}(t),t)dt, \tag{3.1}$$

where $L(\mathbf{x}(t),\mathbf{v}(t),t)$ is the Lagrangian of an electron, is recorded and used for weighting of the final states.

In general this method requires much larger sets of initial states and have not been explored in the present work. In the next sections we will describe the Reihold-Falcón method step-by-step in the context of how it has been applied in this work. The section ends with a review of related, and more advanced, applications.

3.1 Initial states

Initial atomic states for electron in a static nucleus potential are represented by the microcanical distribution in an available specific volume $\nu(\mathbf{r})$. Possible spatial coordinates are determined by the conservation law for energy and the assumption, that kinetic energy $E_k = p^2/2\mu$ cannot be negative,

$$E_k = E_0 - V(\mathbf{r}) \geq 0 \tag{3.2}$$

Here $\mu \approx 1$ a.u. is the reduced mass of the two-body system, $\mathbf{p}$ is the magnitude of momentum and $V(\mathbf{r})$ is the Coulomb potential. Further more, E_0 is the initial energy determined by the Bohr condition 1.1. Therefore the maximal value for the position of an electron r_{max} is given by the condition

$$E_0 - V(\mathbf{r}) = 0 \tag{3.3}$$

Assuming that the above equation has only one root confines the size of the allowed radii interval to $0 < r < r_{max}$. The distribution of initial states are selected from the microcanonical distribution

$$\rho(\mathbf{r},\mathbf{p},E) = D\; d^3r\; d^3p\; \delta(E_0 - E) \tag{3.4}$$

where the system energy $E = E_k + V(\mathbf{r})$, D is a constant depending only on the available volume $\nu(\mathbf{r})$. This function has $6N$ dimensional support and the delta function peaks when $E = E_0$. Therefore we obtain restrictions on the available volume enclosed by the energy hyperspace E_0. The transformation to spherical coordinates reads

$$d^3r d^3p \rightarrow r^2 dr\; d(\cos(\theta_r))\; d\phi_r\; p^2\; dp\; d\cos(\theta_p)\; d\phi_p \tag{3.5}$$

While momentum p and radius r are non-uniformly distributed, angles θ_r, θ_p are spread over half-sphere $\theta \in <0,\pi>$. The azimuthal angles ϕ_r, ϕ_p are uniformly distributed in whole sphere $\phi \in <0,2\pi>$. What remains is the distribution of (r,p) described by the integral,

$$\delta(E - E_0)\; p^2 dp\; r^2 dr \tag{3.6}$$

By using the substitution $p^2 dp = p\;\mu\; dE$, since $E = p^2/(2\mu) + V(r)$ we require,

$$\int_0^E p\mu\,\delta(E - E_0) dE = \mu\; p(E_0, r) \tag{3.7}$$

where $E_0 \in (0,E)$ and $p(E_0) = \sqrt{p(E_0) 2\mu(E - V(r)}$. Finally, we rewrite $\omega(r)$ in terms of only r-coordinate and initial condition E_0,

$$\omega(r,E_0) = \int_0^{r_{max}} \mu\; p(E_0,r')\; r'^2 dr' \;= \int_0^{r_{max}} \rho(E_0,r') dr' \tag{3.8}$$

Fixing the momentum as $p(E_0, r)$, secure radii within the interval $\langle 0, r_{max} \rangle$. Therefore $\omega(r, E_0)$ is uniformly distributed on the interval $\langle 0, \omega_{r_{max}} \rangle$. A random selection then allows for the computation of spatial coordinates

$$\begin{aligned} x &= r(\omega)\ \sqrt{1-t_r}\ \cos(\phi_r) \\ y &= r(\omega)\ \sqrt{1-t_r}\ \sin(\phi_r) \\ z &= r(\omega)\ t_r \end{aligned} \tag{3.9}$$

and momentum coordinates as

$$\begin{aligned} p_x &= p(r(\omega))\sqrt{1-t_p}\ \cos(\phi_p) \\ p_y &= p(r(\omega))\sqrt{1-t_p}\ \sin(\phi_p) \\ p_z &= p(r(\omega))\ t_p \end{aligned} \tag{3.10}$$

Thus we have reduced the $6N-6$ dimensional phase-space to the space defined only by $\omega(r)$ and random angle $\phi(r)$ on r-sphere and p-sphere respectively. The orbital momentum is a pseudovector defined by $\mathbf{l} = \mathbf{r} \times \mathbf{p} = -\mathbf{r} \times -\mathbf{p}$, which is symmetric to the inverse operation. The components are

$$\begin{aligned} l_x &= y \cdot p_z - z \cdot p_y \\ l_y &= z \cdot p_x - x \cdot p_z \\ l_z &= x \cdot p_y - y \cdot p_x \end{aligned} \tag{3.11}$$

The magnitude of the angular momentum is $l^2 = {l_x}^2 + {l_y}^2 + {l_z}^2$. In our calculations, the microcanonical distribution of position is confined by setting the angular momentum in z.direction from $l_z - 0.5$ to $l_z + 0.5$, which reflects a quantum uncertainty in l_z vs. l.

As an example, we compare in Fig. (3.1) the radial distribution of initial states for a 1s and a 9d state of hydrogen. We observe that the classical distributions vanish at the classical turning point $2n^2$ as expexted, while the quantum mechanical densities does not. Apart from that, the two distributions are on an order of magnitude view in agreement. It is in general seen to be quite different from the quantum mechanical probability distribution. Nevertheless we have a distribution of stable initial states of the same order of magnitude as the quantum distribution and from that starting point the outcome of classical calculations may be invoked and compared to quantum calculations.

In the first scientific work of this thesis we consider a one-dimensional (1D) model problem. This require a slight modification of the 3D procedure above. Consider now a single spatial variable (z) and the momentum (p). The microcanonical distribution becomes,

$$D\ dz\ dp\ \ \delta(E(z,p) - E_0) \tag{3.12}$$

Compared to the 3D-case, the terms $r^2\ dr$ and $p^2\ dp$ become simply dz and dp and therefore 1D microcanonical distribution w is computed from the form

$$w(z) = \int_0^z \frac{\mu}{p(z')}\ dz' = \int_0^z \frac{\mu}{\sqrt{2\mu(E_0 - V(z'))}}\ dz' \tag{3.13}$$

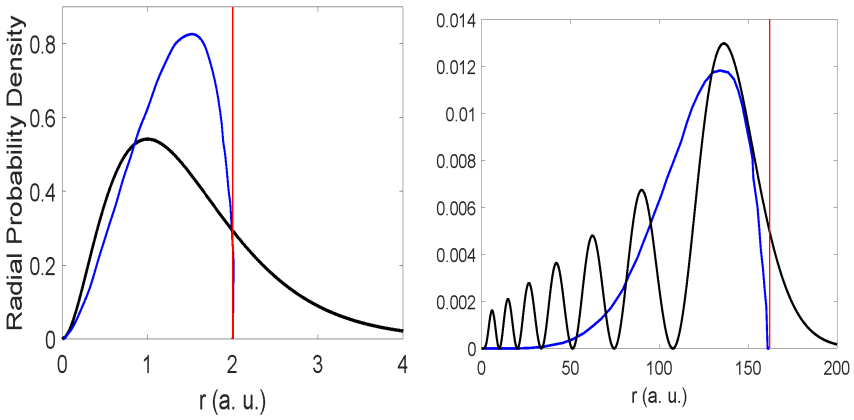

Figure 3.1: Comparison of the 3D-CTMC microcanonical distribution and quantum (black solid line in a.u.) probability density $|\Psi(r)|^2$ for initial states 1s (left) and 9d (right). The vertical red asymptote shows the classical turning point $2n^2$.

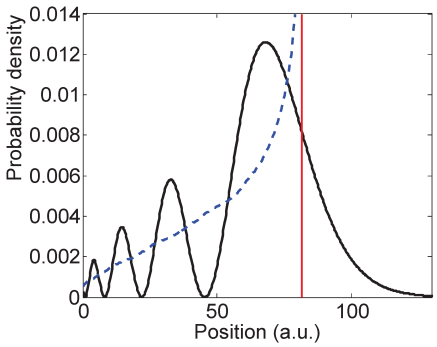

Figure 3.2: 1D-CTMC electron microcanonical distribution for initial states 9d in the positive-half of x-coordinate showing as dotted blue line. The solid black line shows quantum mechanical electron probability density $|\Psi_r|^2$ spreads over positive-half x-coordinate in set-up potential described in [34]. Red vertical asymptote shows classical turning point.

In Fig. (3.2) the classical 1D distribution is compared with a quantum distribution of the 9th excited states. Due to the 1D space the classical distribution diverges at the turning point. Apart from that and again as in 3D, it compares relatively well with the quantum state.

3.2 Dynamics and Final State Analysis

With a set of initial conditions at hand we can propagate each set of electron coordinates under influence of the Coulomb force from the nucleus and the Lorentz force from the electromagnetic

field, in this case,

$$\frac{d\mathbf{r}}{dt} = \frac{\mathbf{p}}{\mu}$$
$$\frac{d\mathbf{p}}{dt} = -\frac{1}{r^2}\mathbf{e}_r + \mathbf{E} \tag{3.14}$$

We observe that these equations takes the form of a coupled first order differential equations, which can be expressed in vector form

$$\frac{d}{dt}\mathbf{a} = \mathbf{b}(t, \mathbf{a}) \tag{3.15}$$

The 6 (3D) or 2 (1D) equations are solved numerically for arbitrary number of initial states using numerical methods described in the next chapter. In the end of the propagation we obtain a series of positions and momenta at every time-step of the propagation.

For illustration we select two single initial states of 9d and plot the trajectory of electron under the driving field. In the Fig. 3.3 the field is 1 kV/cm and and the electron is seen to remain around the nucleus for all times, only being slightly perturbed by the electromagnetic field. In Fig. 3.4 the pulse strenght is much stronger, 360 kV/cm, and the electron is seen to be ionized after just a few trajectories around the nucleus. When ionized it propagates along the negative z-direction before it turns and is accelerated in the positive direction in accordance with the given pulse shape, cf. Eq. (2.41)

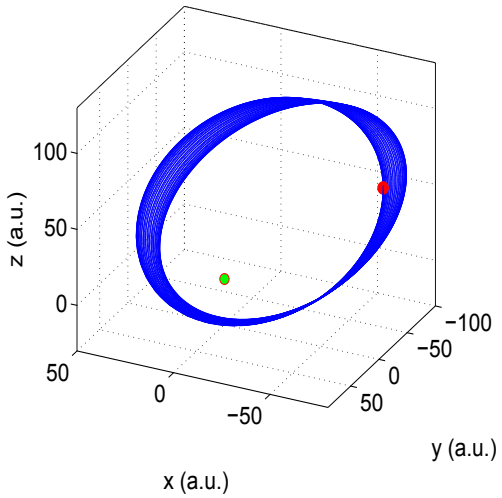

Figure 3.3: The calculated CTMC trajectory (left) as it developed in time for the initial state 9d under a single cycle THz field with strength $E_0 = 1$ kV/cm. The nucleus is shown as the green augmented point at $[0,0]$ and the starting point at t_0 as the red point.

The disitribution of final state position for a large number of initial states in terms of the final (z,r) coordinates are should in Fig. (3.4). The blue dots correspond to initial states which remains bounded after the pulse, the black dots are ionized ones with final energy $E \geq 0$. Note the tendency of ionized electrons to end up with positive z-values. The electrons with largest z-values comes from ionization in the second half cycle. The lowest z-values of ionized electrons originate from situations where the elecron is ionized in the first half cycle.

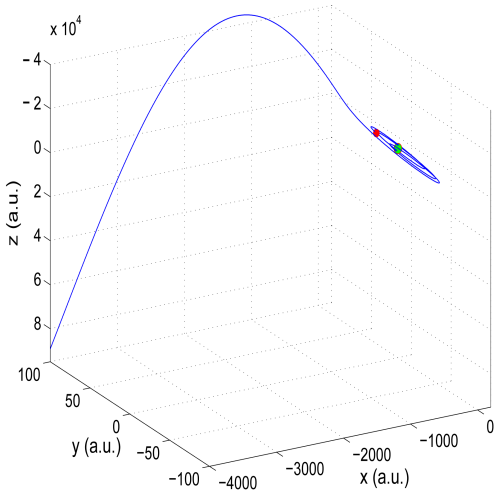

Figure 3.4: The calculated CTMC trajectory (left) as it develope in time for the initial state 9d under single cycle THz field with strength $E_0 = 360$ kV/cm. The nucleus is shown as the green augmented point at $[0,0]$ and the starting point at t_0 as the red point.

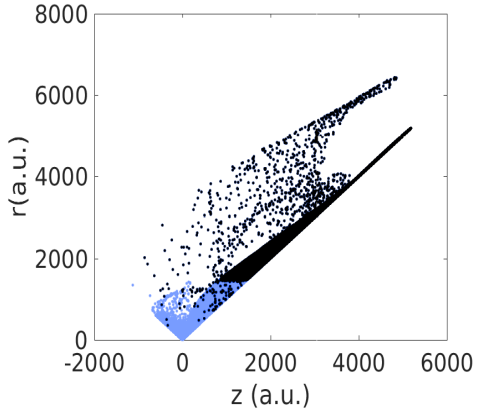

Figure 3.5: Map in (r,z) of final states for initial n=5000 states and 50% of ionization probability. Black dots shows ionized states.

Chapter 4

Numerical methods

In this chapter we will review numerical methods for time propagation which has been applied at various stages during the course of this work. It includes numerical schemes for 1D and 3D quantum and classical dynamics. The first three sections describe algorithms to propagate the TDSE only. The final section describes methods to solve coupled first order differential equations on the form of Eq. (3.15). As described in Chapter 1, an approximate solution of the TDSE at small time-step Δt after the time t_0 can be approximated as

$$\psi(\mathbf{r}, t = t_0 + \Delta t) \simeq \psi(\mathbf{r}, t_0) e^{-i\hat{H}\Delta t} \tag{4.1}$$

Here the wave function (vector) $\psi(\mathbf{r}, t_0)$ describes the state at $t = t_0$. When this state is known, the challenge is to apply the best possible approximation for the exponential operator in front. What is "best" may depend on the structure of the Hamiltonian, the initial state and the problem parameters (integration time, field strength etc.).

4.1 Three-point finite difference method

The discretization of the space-time allow us to compute the wavefunction on a grid. A family of methods called the finite-difference method (FDM) take advantage of this procedure. A derivative at one point is approximated by the differentiate operator computed from the neighbourhood grid-points. The time is dicretized in the interval $\langle t_0, ..., t_{end} \rangle$ and we approximate the first-order derivative in time as the differentiation

$$\frac{\partial \psi(\mathbf{x}, t)}{\partial t} = \lim_{\Delta t \to 0} \frac{\psi(t + \Delta t, \mathbf{x}) - \psi(t, \mathbf{x})}{\Delta t} \tag{4.2}$$

We then obtain the solution in the next time-step $\psi(t + \Delta t, \mathbf{x})$ from the previous step $\psi(t, \mathbf{x})$. First we expand a function as the Taylor series

$$\psi(t + \Delta t, \mathbf{x}) = \psi(t, \mathbf{x}) + \Delta t (\frac{\partial \psi(t, \mathbf{x})}{\partial t}) + \mathscr{O}(\Delta t) \tag{4.3}$$

The forward scheme in combination with the backward scheme

$$\psi(t - \Delta t, \mathbf{x}) = \psi(t, \mathbf{x}) - \Delta t (\frac{\partial \psi(t, \mathbf{x})}{\partial t}) + \mathscr{O}(\Delta t) \tag{4.4}$$

results in the more accurate central difference method based on one forward and one backward step, also called the two-step Euler method

$$\frac{\partial \psi(t, \mathbf{x})}{\partial t} = \frac{\psi(t + \Delta t, \mathbf{x}) - \psi(t - \Delta t, \mathbf{x})}{2\Delta t} + \mathscr{O}(\Delta t^2) \tag{4.5}$$

Adding the two equations together results in the three-point method as

$$\psi(t+\Delta t,\mathbf{x}) = \psi(t-\Delta t,\mathbf{x}) - 2i\hat{H}\Delta t\,\psi(t,\mathbf{x}) \tag{4.6}$$

This 1D-scheme can be extended for y and z coordinates and a similar procedure can be applied to discretize the space variable. This approximation is stable and of second order accuracy in Δt. However, it requires generally very small time steps to remain stable [40]. In addition it is extremely well conditioned for parallelization.

4.2 Crank-Nicolson method

A stabilized FDM is the implicit Cranck-Nicolson method (CN) [41], which combines Euler's forward time-step with the backward time-step method. The CN time-evolution operator is derived from the 1st order expansion of the exponential series of the evolutionary operator

$$\hat{U}(t_{k+1},t_k) \simeq \hat{I} - i\Delta t\hat{H} \tag{4.7}$$

for small Δt. The inverse operator correspondingly becomes,

$$\hat{U}^{-1}(t_{k+1},t_k) \simeq \hat{I} + i\Delta t\hat{H} \tag{4.8}$$

Then, the forward time step is given explicitly as

$$\psi(t_{k+1/2},\mathbf{x}) = [\hat{I} - i\frac{\Delta t}{2}\hat{H}(t_{k+1/2})]\,\psi(t_k,\mathbf{x}) \tag{4.9}$$

Since we want to reverse the time-evolution operator, the full step

$$\psi(t_{k+1},\mathbf{x}) = \hat{U}(t_{k+1},t_{k+1/2})\hat{U}(t_{k+1/2},t_k)\psi(t_k,\mathbf{x}) \tag{4.10}$$

can be rewritten,

$$\hat{U}^{-1}(t_{k+1},t_{k+1/2})\psi(t_{k+1},\mathbf{x}) = \hat{U}(t_{k+1/2},t_k)\psi(t_k,\mathbf{x}) \tag{4.11}$$

Using the first order approximation for the time development operators we obtain the numerical scheme called the Cranck-Nicolson method or sometimes the Cayley-propagator,

$$\left[1 + i\frac{\Delta t}{2}\hat{H}(t_{k+1/2})\right]\psi(t_{k+1},\mathbf{x}) = \left[1 - i\frac{\Delta t}{2}\hat{H}(t_{k+1/2})\right]\psi(t,\mathbf{x}) \tag{4.12}$$

Representing ψ on as a vector with reference to a basis we obtain $\hat{H}$ as a matrix. The first step on the right side becomes a matrix-vector multiplication and the final step requires a matrix inversion. The implicit CN method is unconditionally stable and accurate up to $\mathscr{O}(\Delta t^3)$. However, the matrix inversion is generally time consuming unless the matrix is sparse.

4.3 Split-operator operator Fourier method

While the previous methods are well suited for 1D problems, they fast become intractable to 3D models. The reason is the replacement by the second derivative with the full Laplacian operator. An alternative is then to take advantage of basis expansions in terms of spherical harmonics and combine that with a representation of the radial expansion coefficients in the momentum space and the Fast Fourier Transform (FFT) algorithm. In 1D the expansion in spherical harmonics

can be omitted and we discretize space in $x \in \langle x_0..x_N \rangle$ uniformly with $N = 2^n$ points. In the momentum space we correspondingly obtain, $p \in \langle k_0..k_N \rangle$. The discrete points in p-space are related to the x-discretization as

$$k_n = \frac{2\pi}{n\Delta x}, n = -N/2, -N/2+1, ..., N/2 \tag{4.13}$$

The wave function in the momentum space can now be computed as the FFT of the wavefunction in the coordinate space and vice versa,

$$\widetilde{\psi}(k_n) = \hat{F}\psi(x) = \Delta x \frac{1}{\sqrt{2\pi}} \sum_{m=0}^{N} e^{-ik_n x_m} \psi(x_m) \tag{4.14}$$

Here F denotes the Fourier transformation. The inverse Fourier transformation gives back the wave function in the coordinate space

$$\psi(x_m) = \hat{F}^{-1}\widetilde{\psi}(k_n) = \Delta p \frac{1}{\sqrt{2\pi}} \sum_{n=0}^{N} e^{ik_n x_m} \widetilde{\psi}(k_n) \tag{4.15}$$

Note that the Fourier transformation is unitary, ie. $\psi(\mathbf{x})$, since Fourier transformation is the unitary transformation $\hat{F} \times \hat{F}^\dagger = 1$. The time evolution operator contains kinetic and potential energy operators is now split into two terms

$$\hat{U}(t+\Delta t, t) \simeq \exp(-i\hat{T}\Delta t)\exp(-i\hat{V}\Delta t) \tag{4.16}$$

which introduce a splitting error of second order, $\mathscr{O}(\Delta t^2)$. A more accurate expression is a separation of one of the operator, here kinetic operator, in two half steps

$$\begin{aligned} \hat{U}(t+\Delta t/2, t) &\simeq \exp(-i\hat{T}\Delta t/2)\exp(-i\hat{V}\Delta t/2) \\ \hat{U}(t+\Delta t, t+\Delta t/2) &\simeq \exp(-i\hat{V}\Delta t/2)\exp(-i\hat{T}\Delta t/2) \end{aligned}$$

The product of these two expressions gives for a full step

$$\hat{U}(t+\Delta t, t) \simeq \exp(-i\hat{T}\Delta t/2)\exp(-i\hat{V}\Delta t)\exp(-i\hat{T}\Delta t/2) \tag{4.17}$$

which has an error of order $\mathscr{O}(\Delta t^3)$. The trick is now to let each exponential operator work separately and perform FFT of the wavefunction before each operation with the kinetic term.

$$\psi(t+\Delta t, \mathbf{x}) = \hat{F}^{-1}\left[e^{-i\hat{T}\Delta t/2}\hat{F}\left[e^{-iV(t)\Delta t}\hat{F}^{-1}\left[e^{-i\hat{T}\Delta t/2}\hat{F}\psi(t,\mathbf{x})\right]\right]\right] \tag{4.18}$$

The main advantage of the split-operator technique is that, in momentum space, the kinetic part of the evolution operator is diagonal. Thus, having performed the FFT the operator is directly computed as $\exp(-i\hat{T}\Delta t/2)\widetilde{\psi}(k_n)$. The method of computing FFT is well known and grows quasilinearly $\mathscr{O}(N\log N)$. In 1D, the propagation of the potential operator is diagonal in position space so the operation is linear in N. In 3D, this step often imply a matrix - vector multiplication, $\mathscr{O}(N^2)$, and thus becomes the most time-consuming.

4.4 Split-operator operator Fourier method in spherical coordinates

A split-step method in spherical coordinates for central symmetric problems was developed by Herrmann and Fleck [42] and extended to general 3D problems in [43]. The idea is to expand the

wavefunction in radial grid functions augmented by spherical harmonics and take the advantage of the spherical Hamiltonian for the reduced wavefunction

$$\hat{H} = \left[\frac{1}{2}\frac{\partial^2}{\partial r^2} + \frac{\hat{L}^2}{2r^2} + \underbrace{V(r) + E(t)\cdot \mathbf{r}}_{\tilde{V}(r,\Omega,t)} \right] \tag{4.19}$$

where $\hat{L}$ is the angular momentum operator, $V(r)$ is a spherical symmetric potential and $E(t)$ is a time-dependent external field.

The grid expansion of the reduced function then reads, with m_l conserved for z-polarised pulses,

$$\psi(r,\Omega,t) = \sum_{l=0}^{l_{max}} f_l^{m_l}(r,t) Y_l^{m_l}(\Omega) \tag{4.20}$$

The split step scheme takes the form

$$\psi(r,\Omega,t_{n+1}) = \hat{F}^{-1}\left[e^{-i\frac{\partial^2}{\partial r^2}\frac{\Delta t}{4}} \hat{F} e^{-i\tilde{V}(r,\Omega,t)\Delta t} e^{-i\frac{\hat{L}^2}{2r^2}\Delta t} \hat{F}^{-1}\left[e^{i\frac{\partial^2}{\partial r^2}\frac{\Delta t}{4}} \hat{F}\psi(r,\Omega,t_n)\right]\right] \tag{4.21}$$

The FFT step now acts only on the basis in momentum space as in 1D. After transforming back to r-space the second operator applies,

$$e^{\frac{-i\hat{L}^2}{2r^2}\Delta t} \sum_{l=0}^{l_{max}} f_l^{m_l}(r_i) Y_l^{m_l}(\Omega_j) \longrightarrow \sum_{l=0}^{l_{max}} f_l^{m_l}(r_i) e^{\frac{-i\Delta t l(l+1)}{2r^2}} Y_l^{m_l}(\Omega_j) \tag{4.22}$$

and from this expression the full wavefunction $\psi(r_i,\Omega_j,t_k)$ is constructed on a grid. Then, any spatial dependent potential may be multiplied directly,

$$e^{-i\tilde{V}(r_i,\Omega_j,t)\Delta t)}\psi(r_i,\Omega_j,t) \longrightarrow \psi(r_i,\Omega_j,t+\Delta t) \tag{4.23}$$

From this new wavefunction we can obtain the iterated radial basis functions by projection,

$$f_l(r_i,t+\Delta t) = \int d\Omega\, Y^{*m_l}_{\ l}(\Omega)\psi(r_i,\Omega,t+\Delta t) \tag{4.24}$$

The projection is accurately performed with Gauss-Legendre sum of of l_{max} points. Now, the final FFT transformation and kinetic evolution operator is carried out on these iterated basis functions and one step has been completed.

4.5 Split-operator operator Fourier method in cylindrical coordinates

The set of cylinder coordinates is far from an obvious choice for Coulomb problems alone, since this set of coordinates does not offer separability and analytical basis states. However, for cases where a linear z-polarised field drives the dynamics essentially along this axis, this set of coordinates can be effective. As another advantage, it offers the possibility to switch between length and velocity gauge with minumum amount of programming work. A complication is the need to transform initial and final states to and from cylindrical coordinates before and after computations. The method to be presented was formulated by Chelkowski et. all [44]. We here

follow their description and additionally show how it can be formulated in both gauges. The implementation of this work was performed towards the end of the PhD project, so it has not yet been directly applied in calculations leading to new scientific results. However, the present section ends with first 3D results of the 1D calculations published in paper III.

In cylindrical coordinates (z,ρ,ϕ) the Coulombic potential for hydrogen is given as

$$V(\rho,z) = -\frac{1}{\sqrt{\rho^2+z^2}} \tag{4.25}$$

The Laplacian operator contains the partial derivation of both, ρ and z coordinates and the TDSE takes the form

$$\left[-\frac{1}{2}\frac{\partial^2}{\partial z^2} + D_\rho + V(\rho,z) + zE(t) - i\frac{\partial}{\partial t}\right]\psi(z,\rho,t) = 0 \tag{4.26}$$

where the the interaction term is written in the length gauge and the term with D_ρ is the part of the kinetic operator in the ρ coordinate,

$$D_\rho = -\frac{1}{2}\frac{\partial^2}{\partial\rho^2} - \frac{1}{2\rho}\frac{\partial}{\partial\rho} \tag{4.27}$$

The starting point is an expansion in basis functions related to the D_ρ operator,

$$\nu_n(\rho) = \frac{2^{1/2}}{LJ_1(x_n)}J_0(x_n\rho/L) \tag{4.28}$$

where J_0 and J_1 are Bessel functions, x_n are zero points of J_0 and L is the size of the box in the ρ-direction. The basis has the property,

$$D_\rho\nu_\rho = (x_n/L)^2\nu_n(\rho) \tag{4.29}$$

and form an orthonormal set of states. Performing the expansion

$$\psi(z,\rho,t) = \sum_{n=0}^{N} f_n(z,t)\nu_n(\rho) \tag{4.30}$$

and projecting out on each basis state result in a coupled set of differential equations (in time and z),

$$i\frac{\partial f_n(z,t)}{\partial t} = \left[-\frac{1}{2}\frac{\partial^2}{\partial z^2} + V(z) + E(t)z\right]f_n(z,t) \tag{4.31}$$

where $\mathbf{V}(z)$ is a square non-singular matrix with elements

$$V_{n,m}(z) = (x_n/L)^2\delta_{n,m} + \int_0^L \nu_n V_c(\rho,z)\nu_m\rho d\rho \tag{4.32}$$

which has to be precalculated and stored. Note that this is a time independent operator so the calculation is only performed once. The split step procedure takes the form, with $D_z = \partial^2/\partial z^2$,

$$\psi(z,\rho,t+\Delta t) = \hat{F}^{-1}e^{-iD_z\Delta t/4}\hat{F}\left[e^{-iE(t)z\Delta t/2}e^{-i\mathbf{V}(z)\Delta t/2}\hat{F}^{-1}\left[e^{-iD_z\Delta t/4}\hat{F}\phi(z,\rho,t)\right]\right] \tag{4.33}$$

The coupling between different f_n functions takes place in the second operator. Note that it only requires a matrix-vector operation of an (N,N) sized matrix and a vector of length N. This is a

large advantage as compared to the spherical scheme. In velocity gauge we simply put the field interaction into momentum space and obtain, with $p_z = -iS\partial/\partial z$,

$$\psi(z,\rho,t+\Delta t) = \hat{F}^{-1} e^{-iD_z\Delta t/4} e^{-iA(t)p_z\Delta t/2} \hat{F} \left[e^{-i\mathbf{V}(z)\Delta t/2} \hat{F}^{-1} \left[e^{-iA(t)p_z\Delta t/2} e^{-iD_z\Delta t/4} \hat{F} \phi(z,\rho,t) \right] \right] \tag{4.34}$$

We have applied this method to reconsider the possibility to translate wavefunctions in single cycle pulses, cf. Paper III. In the figure below we reproduce initial and final states for the two cases of Fig. 4 in that paper. Indeed the wavefunction is seen to be translated without distortion for initial 10s, while the 1s state is "destroyed". It is also noteworthy to observe how similar in shape the distorted final 1s state in 3D compares with the 1D result.

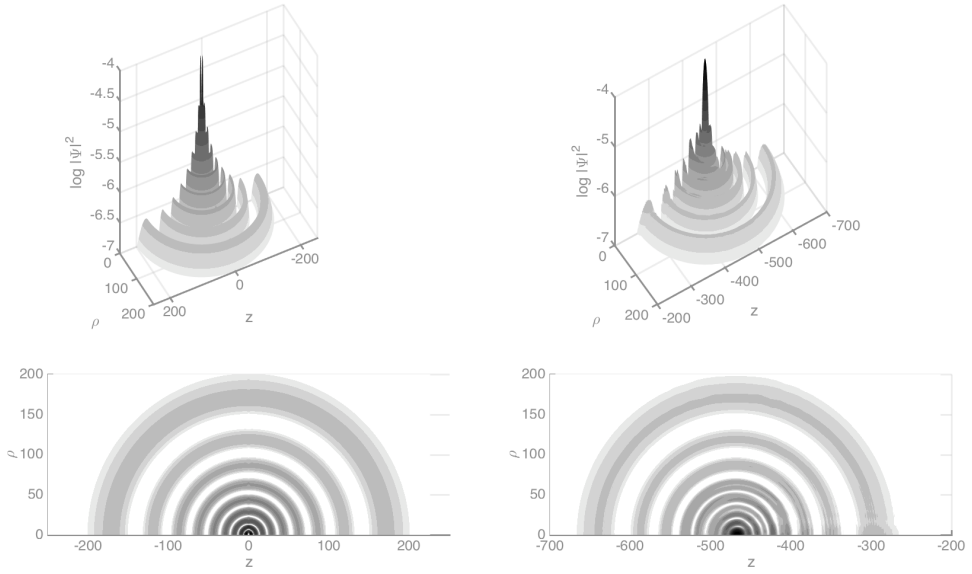

Figure 4.1: Probability density of the intial state (left) and the state after time propagation (right), plotted on logarithmic scale. The full scale is 3 decades, grey color scale with five shades per decade. The upper version are 3D surface plots in the ρ-z plane, the lower is a plane projection. The pulse is coming from the right in the upper part. (This picture was provided by prof. L. Kocbach, IFT, UiB).

4.6 Propagation of Classical Dynamics

In propagating the classical dynamics we have applied both high order and low order numerical schemes. The lowest order schemes can be directly implemented with small time steps. The first order derivative for the position updates to

$$r(t_{i+1}) - r(t_i) = \int_{t_i}^{t_{i+1}} \mathbf{v}(t')\, dt' \approx v(t_i)\, \Delta t \tag{4.35}$$

The Euler's method is computed with linearly distributed time steps over all intervals and estimated error is roughly the size of the time step interval Δt. We can include the second order

derivatives in Taylor's expansion of a searched function, which gives a smaller error of the order Δt^2, if $\Delta t << 1$. The velocity may be updated at intermediate half time steps,

$$v(t_{i+1/2}) = v(t_{i-1/2}) + \frac{F(t_i)}{\mu}\,\Delta t \tag{4.36}$$

This substitution leads to the three-step Euler method also called the midpoint method. The midpoint method gives better approximation of solution with the complexity $\mathcal{O}(\Delta t^3)$. Another method for integrating differential equations is Verlet's algorithm developed by Loup Verlet in the 1960s [45]. We start with the Newton's equation of motion for electron

$$\frac{d^2\mathbf{r}}{dt^2} = \frac{\mathbf{F}}{\mu} \tag{4.37}$$

which we can replace by the three-point formula 4.36 of second order derivative

$$\left.\frac{d^2\mathbf{r}}{dt^2}\right|_{t=t_i} = \frac{1}{\Delta t^2}(r_{k+1} - 2r_k + r_{k-1}) \tag{4.38}$$

Putting above equations together we get

$$r_{k+1} = 2r_k - r_{k-1} + \Delta t^2 F_k \tag{4.39}$$

In practice we know initial position r_0 and velocity v_0 , so the first step is to find r_1 to start the recursion.

$$r_1 \simeq r_0 + \Delta t v_0 + \frac{\Delta t^2}{2} F_0 \tag{4.40}$$

where the force is calculated as $\mathbf{F} = -\boldsymbol{\nabla} V(\mathbf{r}) - E(\mathbf{r})$. Since Verlet's integration technique use several past steps to estimate a current value, it is a sort of the multi-step method. Verlet's algorithm, as well as Newton's equations, is numerically stable and reversible in time.

Runge-Kutta's solvers (RK) use only one previous step to calculate the current value of a searched function. Furthermore the time interval is non-uniformly divided into smaller parts, according to the order of RK, to minimize the approximation error. As the time step are divided by halving the original time interval, a slope of a searched function are divided into nodes with different weights in each node to better approximate it. Coefficients for nodes are documented in a relevant literature [46]. Let us assign time-step as $h = \Delta t$, RK of the 4-th order (RK4) estimates solution in radial coordinate as

$$v(h+1) = r(h) + \frac{h}{6}(k_1, 2k_2, 2k_3, k_4) \tag{4.41}$$

with slopes in each node $k1 - k4$ given as

$$\begin{aligned} k_1 &= v(r(h), h) \\ k_2 &= v(r(h) + \frac{h}{2}\,k_1, h + h/2) \\ k_3 &= v(r(h) + \frac{h}{2}\,k_2, h + h/2) \\ k_4 &= v(r(h) + h\,k_3, h) \end{aligned} \tag{4.42}$$

The low order methods was applied for test calculations of 1D CTMC. The simple programming makes it possible to take advantage of the spike in the potential at $r = 0$, cf. paper I. In 3D we

have applied the Runge-Kutta-Fehlberg of 4/order 5 embedded pair method (RKF45) [46]. The error estimation is most often estimated by running the ODE solver of higher order in parallel with the lower order of RK. For RKF45, the solution of the 4th-order is compared with the 5th order solution. By substracting these two solutions at each time step, one can get a local truncation error estimation $e(i)$. Advanced implicit methods as RKF45 check the step size based on the truncation error during the propagation in order to get converged results.

Chapter 5

Scope of the work

Electromagnetic pulses can be produced with a broad range of frequencies, intensities and pulse lengths. The strongest pulses produced so far have intensities many orders of magnitude above the intensity defined by the field strength of the ground state hydrogen atom [1], $\sim 10^{21}$ W/cm^2 in Rutherford Appleton Laboratory [47].

The shortest pulse lengths are attosecond pulses, high frequency pulses of duration 43 attoseconds [48]. The "standard" pulses of strong field physics are 400-1600 nm wavelengths reaching peak intensities around 10^{14} W/cm^2 and having a pulse length of the order 10 fs. Such pulses contains a number, typical 2-10 optical cycles. This implies that for linear polarized fields the atom is exposed to a time dependent oscillating field with a corresponding lowering of the potential barrier, cf. Fig. 5.1.

Several competing processes can lead to ionization. First of all the electron may instantaneously or sequentially absorb a number of photons which cause multiphoton ionization. With a central pulse frequency ω_0, a binding energy ε_0 the electron will appear in the continuum with the energy $\varepsilon = N\omega_0 - \varepsilon_0$, illustrated as process III in Fig. 5.1. Another process is tunneling ionization. Here electron tunnel through the barrier and propagate in the continuum as illustrated by process I. As the field changes direction, electron may be accellerated back towards the nucleus, collide with the remaining part of the wavefunction and ionize. Alternatively it may be recaptured by the nucleus and release a high frequency photon containing the energy gained in the continuum. This is the origin of High Harmonic Generation. Finally, it may happen that the electron after tunneling populate a combination of states, which ionize directly without recombination. For tunnelling ionization to be effective, the frequency needs to be small, in contrast to multiphoton ionization which is most effective for high frequency photons. The process was first analyzed by Keldysh in 1965 [49]. He introduced a parameter γ_k which classify the dominant ionization mechanism

$$\gamma_k = \sqrt{\frac{I_p}{2U_p}} = \sqrt{\frac{2I_p\omega^2}{E_0^2}}, \tag{5.1}$$

where I_p is the atom ionization energy, $U_p = E_0^2/(4\omega^2)$ is the ponderomotive energy of the electromagnetic field with amplitude E_0 and frequency ω. It is the energy gained by an free electron in a harmonically oscillating field. As we consider the field strength of $10^{-4} - 10^{-5}$ a.u. and ω = 2.3510^{-5} a.u., in our case $\gamma_k << 1$. Tunneling ionization generally dominates over multiphoton ionization when $\gamma \ll 1$. A final process, marked as II in Fig. 5.1 is "over the

[1] E = 5.1×10^9 V/cm at r = a_0

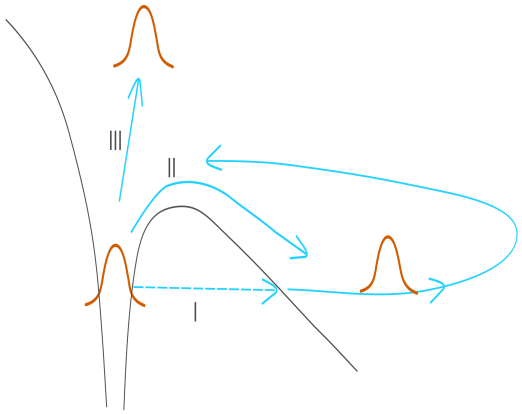

Figure 5.1: Processes in strong field ionization. I. Tunneling ionization with possible driving of electron back to the nucleus. II. Over the barrier ionization and III. Multiphoton ionization

barrier" ionization. It follows as a natural extension of tunneling, which is 'under the barrier' ionization, for sufficiently strong fields. At that point, the barrier has been lowered below the energy level of the particle in question and it may be directly accelerated along the negative field direction. For a slowly increasing field strength, the ionization process may well first start out as process I and terminate as process II.

Ionization by strong single cycle pulses needs some modifications of the standard process map above. Indeed, all three processes may take place. However, the single cycle nature of the mechanism may prohibit the recollision process. First of all, an initially free electron at the rest will first be accelerated opposite the field direction and then decelerated and brought to the rest a final distance given by the displacement parameter $\alpha(T)$, cf. Chapter 2. The reason is caused by the fact that laser pulses carries zero DC component, $\int E(t)dt = 0$, when integration is taken over the entire pulse. Unlike multicycle pulses single cycle pulses imply a nonzero displacement, $\int A(t)dt \neq 0$. This imply that the electron tends to be translated by the pulse. Consider for example the pulse shape 2.41. If the electron is ionized in the first half cycle the field will accelerate the particle in the negative z-direction until the electric field has turned and accelerate the particle back towards the nucleus and a recollision modified ionization process may occur. On the other side, the first cycle may simply be too week to cause any significant ionization. The particle remains bound and dressed by the field until the strongest field strengths occur. The electron may here be released and directly accelerated towards positive z-direction. If both processes occur simultaneously, the two processes interfere and the final result needs a careful quantum mechanical treatment.

In the following we will discuss scaling phenomena in the ionization process.

A scaling law is here defined in the following way: Consider a process $P = P(x,y)$ which depends on two parameters x,y. The process displays a surface in terms of x and y, but may also be represented as a number of curves for certain values of $y = y_n$. $P(x) = P(x;y_n)$. The scaling hypothesis predicts that all curves of this family will collapse onto a single curve provided we consider a scaled P as a function of a scaled x. This means a P divided by some functional relation of x, y_n and a scaled x as function of y_n. In the present work we consider only scaling of the independent variable x, where x is pulse strength or momentum.

In 2014 Li and Jones reported single cycle ionization by excited Na(n,d) atoms in THz fields up to 400 kV/cm pulse strengths [26]. They found a surprising n^{-3} scaling law for the total ionization probability and reproduced the scaling behaviour by CTMC calculations. Thus, plotting the ionization probability against a scaled pulse strength it appears as a universal curve. The surprise comes from the fact that CTMC calculations starting from a bound-state distribution necessary takes place through over-the-barrier processes which would be expected to scale as n^{-4}. In Paper 1 we set out to try to model the process quantum mechanically. A 1D model was chosen to cope with the extremely long integration times of a THz pulse. The results of this model gave an approximate n^{-3} power law dependence. Considering the range pulse strength region where the ionization probability switches from zero to unity and comparing this with the height of the potential barrier we concluded that the dominant mechanism could be ascribed to tunneling. However, the conclusion limited itself to 1D calculations, where the ionization probability as the function of pulse strength itself did not match the experiment very well: Our computed ionization probabilities were rising much more rapidly than the experiments.

This motivated studies of the very same process in 3D. We performed length-gauge calculations based on the split step method described in Chapter 2. Here we could compare our results with calculations performed, mainly at shorter pulse lengths [51, 52]. This group also obtained an almost magical agreement between CTMC and TDSE calculations. Our TDSE calculations agreed very well with their for initial $n = 15$,d states of hydrogen. We then extended their calculations towards the experimental pulse lengths and computed ionization probabilities both with the CTMC and the TDSE methods.

Our results can be summarized as follow:

- The quantum mechanical ionization probabilities fall on a universal curve for a mixed scaling parameter containing elements of n^3 and n^4.

$$E_0^{sf}(n) = \alpha n^{-4} + (1-\alpha)n^{-3} \tag{5.2}$$

  In addition, the much steeper response to the pulse strength than observed in experiments remains. Applying this scaling function to the emitted electron momenta of ionized electrons, we find that all initial states gives characteristic scaled electron momenta.

- The CTMC calculations does not follow the same scaling law, and in the long pulse limit there are significant differences between the final state momentum distributions between the two methods.

- Coulomb phases are important to compute the differential cross section, in particular the low energy tail. Electrons which appear to be propagating in the positive z-direction are affected by the Coulomb phases and appear on the negative side, cf. Fig 7 of Paper II 7.2. A detailed derivation of the differential cross section based on the output of the applied grid method is given in Appendix 2.

Several factors may explain the differences between experiment and theory: Our representation of the experimental pulse shapes and the experimental pulse shape in itself, may not be accurately enough. There may be other experimental factors as well as limits and errors occurring in the numerical results. Therefore we have reported all details of our approach with the hope that future approaches and new experiments can create a complete understanding of this issue.

The final paper III cf. 7.3 of this work was initiated by the research process of testing the spherical code. By accident we discovered that a strong, short single cycle pulse could remove the entire wavefunction from the atom. It turned out that this discovery was done about 13 years ago by Dimitrovsky and coworkers, cf. [50]. We were however able to extend their analysis and point out a few new results:

- The wavefunction is translated completely along the displacement vector.
- Excited atoms are translated almost without dispersion, implying that the removal of the nucleus can offer direct imaging of doubly excited states and dynamical features.

A natural extension of this work would be to confirm the 1D results here obtained with full 3D calculations. In the final stage of the PhD work we developed a split-step method in cylindrical coordinates for this purpose. Test calculations with the same pulses as in paper III agree with the main conclusions from 1D cf. 7.1.

Chapter 6

Conclusion and outlook

In the present thesis we have studied aspects of one-electron dynamics in atoms exposed to a single cycle electromagnetic pulse. The work has implied theoretical analysis, programming, parallel computing on supercomputers and analysis. The focus have been to initially excited atoms and we have considered pulse lengths from significantly longer than the corresponding classical orbital time of the initial state in question to significantly shorter. The focus has been to explore the ionization dynamics in detail, the characteristics of the wavefunction after the pulse including the angular distribution of the emitted electrons. The results are in partial agreement with experiments and independent theoretical works. The agreement amounts to identical quantum mechanical computed results for ionization. Our CTMC results, however, differ from the computed results of [51] and [52]. Neither did we obtain the same scaling law as obtained in the experimental work [26]. One origin of the disagreement may be a different selection procedure for initial states. Regarding experiments we find relatively similar response to the electric pulse with increasing strength. However, the response in our calculations are stronger, or more sensitive to increasing strength. A possible origin of this discrepancy may lie in the experimental knowledge of the pulse. Another origin may be that we use hydrogen d-states, while in experiment was measured with alkali Rydberg-atoms. Only new experiments in combination with independent calculations can settle this issue.

Following the introduction in Chapter 1, Chapter 2 describes the main features of non-relativistic quantum mechanics applied in this thesis. Chapter 3 correspondingly describes the CTMC method we applied. In Chapter 4 we have described numerical methods, which have been tested and applied at various stages in this work. Chapter 5 describes the scope of the scientific work and can be viewed as an introduction to the scientific results in the form of three published papers 7.

Highlighting the results, we mention that a 1D model grasps the main feature of the ionization dynamics. An extension of the work to 3D involved both a new implementation of the spherical split-step method, a new implementation of the split-step method based on cylindrical coordinates and use of an often applied CTMC method. Scaling laws for both, quantum and CTMC calculations of ionization probability and momenta have been found in the long pulse limit. The angular distribution with quantum phases shows possible backward scattering in contrast to the scattering predicted directly from classical calculations. Regarding short intense pulses we showed that the dynamics of a wavefunction is fully described with the translation vector in Kramer-Henneberger frame: This imply that an intense field may “grab“ the entire wavefunction and transfer it far away from its nucleus. We noted that this may be the origin of a potential new imaging technique.

In closing, we mention several routes of extensions of this work. First of all, the response of nano-structures to single cycle pulses is both interesting from the fundamental point and may lead to a new technology. Fundamentally, the ionization dynamics of metallic states contains new aspects. From an applied point of view, scaling laws may be applied to characterize nano-tip fabrications [53]. For atoms, it would be interesting to consider scattering from a series of l states and to investigate the sensitivity to quantum defects in alkali atoms. Exploring pulse shapes which could actually reproduce the experiments in detail would be interesting as well. Finally, a more in-depth study of wavefunction translation would also be very interesting. One may speculate that doubly excited atoms or dynamical processes inside single electron atoms may be explored by wavefunction translative pulses in combination with recording the translated electron spectrum of the atom without nucleus.

Bibliography

[1] J. J. Thomson, Philos. Mag. **44**, 293 (1897). 9

[2] J. J. Thomson Philos. Mag. **40**, 512 (1895). 9

[3] E. Rutherford, Philos. Mag. **21**, 669 (1911). 9

[4] M.Planck, Ann. Phys. **309**, 553 (1901). 9

[5] A. Einstein, Ann.Phys. **17**, 132 (1905). 9

[6] N. Bohr, Philos. Mag. **26**(6), 1-25 (1913). 9

[7] L - V. de Broglie, *Recherches sur la Theorie des Quanta*, Ann. de Phys. 10^e serie, t.III (1925). Translated by A.F. Kracklauer, AFK (2004). 9

[8] C. Davisson and L. H. Germer, Phys. Rev. **30**, 705 (1927). 10

[9] G. P. Thompson, A. Reid, Nature **119**, 890 (1927). 10

[10] P.G. Merli, G.F. Missiroli, G. Pozzi, Am. J. Phys. **44**, 306 (1976). 10

[11] E. Schrödinger, Ann. Physik, **79**, 745 (1926). 10, 12

[12] M. Born, Die Naturwissenschaften **15**, 238 (1927). 10

[13] M. Born, Nature **119**, 354 (1927). 10

[14] K. yon Klitzing, G. Ebert, N. Kleinmichel, H. Obloh, G. Dorda, and G. Weimann, Proc. ICPS **17**, Edited by J. D. Chadi and W. A. Harrison, (Springer, NY, 1985). 10

[15] K. Varju, Y. Mairesse, B. Carre, M. Gaarde, P. Johnsson, S. Kazamias, P. Salieres, J. Mod. Opt. **52**, 379-394 (2005). 10

[16] J. Mauritsson, M. Gaarde, K. J. Schafer, Phys. Rev. A **72**, 013401 (2005). 10

[17] Ch. Brand et al., Nature Nanotechnology **10**, 845 (2015). 10

[18] J. P. Cotter et all, Science Advances **3**, 12017 (2017). 10

[19] I. Lekavicius, D. A. Golter, Thein Oo, Hailin Wang, Phys. Rev. Lett. **119**, 63601 (2017). 10

[20] J. J. Donatelli, J. A. Sethian, P. H. Zwart, PNAS **114**, 7222 (2017). 10

[21] M. V. Dutt, L. Childress, L. Jiang, E. Togan, J. Maze, F. Jelezko, A. S. Zibrov, P. R. Hemmer, M. D. Lukin, Science **316**, 1312 (2007). 10

[22] J.M. Hansteen, O.P. Mosebekk, Nuclear Physics A **201**(3), 541-560 (1973). 11

[23] J. S. Briggs, J. M. Rost, EPJ D **10**, 311-318 (2000). 11

[24] D. Griffiths, *Introduction to Electrodynamics* (Prentice Hall, 1999), ISBN 9780138053260. 11

[25] D. J. Griffiths *Introduction to Quantum Mechanics (2nd ed.), 247*, (Prentice Hall,2004), ISBN 0-13-111892-7.

[26] S. Li, R. R. Jones, Phys. Rev. Lett. **112**, 143006 (2014). 17, 35, 37

[27] T. Birkeland, M. Førre, J. P. Hansen and S Selstø, J. Phys. B: At. Mol. Opt. Phys. **37**, 4205-4219 (2004).

[28] G. Lagmago Kamta, A. D. Bandrauk, Phys. Rev. A **71**, 053407 (2005). 17

[29] N. Metropolis, S. Ulam. J. of the Am. stat. assoc. **44**(247), 335-341 (1949). 19

[30] J. von Neumann, *Monte Carlo Method **12**, 36-38*, Ed. by A.S. Householder, G.E. Forsythe, and H.H. Germond,(Washington, D.C.: U.S. Government Printing Office, 1951). 19

[31] R. A. Abrines, I. C. Percival, Phys. Lett. **13**(3), 216-217 (1964).
R. A. Abrines, I. C. Percival. Proc. Phys. Soc. **88**(4), 861-873 (1966). 19

[32] I. C. Percival, D. Richards, Adv. At. Mol. Phys. **11** (1975). 19

[33] C. O. Reinhold and C. A. Falcón. Phys. Rev. A, **33**(6), 3859-3866 (1986). 19

[34] H. Agueny, M. Chovancová, J. P. Hansen, L. Kocbach, J. Phys. B At. Mol. Opt. Phys. **49**, 245002 (2016). 22

[35] X. Y. Lai, C. Qing-Yu and M. S. Zhan, New J. Phys. **11**, 113035 (2009). 19

[36] Z. Ruan, R. G. Zeng, Y. Ming, M. Zhang, B. Da, S. F. Maod, Z. J. Ding*a, Phys. Chem. Chem. Phys. **17**, 17628-17637 (2015). 19

[37] E. J. Kirkland. *Advanced Computing in Electron Microscopy*, (Plenum, New York, 1998). 19

[38] R. P. Feynman, Rev. Mod. Phys. **20**, 367 (1948). 19

[39] Min Li, Ji-Wei Geng, H. Liu, Y. Deng, Chengyin Wu, Liang-You Peng, Qihuang Gong,and Yunquan Liu, Phys. Rev. Lett. **112**, 113002 (2014).

[40] C. Leforestier et al., J. Comput. Phys. **94**, 59 (1991). 26

[41] J. Cranck and J. Nicholson, Mathematical Proceesings of Cambridge Philosophical Society **43**, 50-67 (1947). 26

[42] Mark R. Hermann and J. A. Fleck, Jr., Phys. Rev. A **38**, 6000 (1988). 27

[43] J. P. Hansen, T. Sørevik, and L. B. Madsen Phys. Rev. A **68**, 031401(R) (2003). 27

[44] S. Chelkowski, T. Zuo, A. Bandrauk, Phys.RevA **46**(9) (2002). 28

[45] L. Verlet, Phys. Rev **159**, 98 (1967). 31

[46] T. Sauer, *Numerical analysis, 2nd edition*, (Pearson Education Limited, 2013). 31, 32

[47] C. Hernandez-Gomez et al, J. Phys.: Conf. Ser. **244**, 032006 (2010). 33

[48] Gaumnitz T, Jain A, Pertot Y, Huppert M, Jordan I, Ardana-Lamas F, Wörner HJ. Optics Express **25**(22), 27506-27518 (2017). 33

[49] V. Keldysh, Sov. Phys. JETP **20**, 1307 (1965). 33

[50] D. Dimitrovski, E. A. Solov'ev and J S Briggs, Phys. Rev. Lett. **93**, 083003 (2004). 36

[51] B. C. Yang and F. Robicheaux, Phys. Rev. A **90**,063413 (2014). 35, 37

[52] B. C. Yang and F. Robicheaux, Phys. Rev. A **91**, 043407 (2015). 35, 37

[53] L. Wimmer, G. Herink, D. R. Solli, S. V. Yalunin, K. E. Erchternkamp and C. Ropers, Nat. Phys. **10**, 432-436 (2014). 38

[54] J. P. Hansen, J. Lu, L. B. Madsen, and H. M. Nilsen, Phys. Rev. A **64**, 033418 (2001). 83

Chapter 7

Scientific Results

List of Papers

I) H Agueny, M Chovancova, J P Hansen and L Kocbach. **Scaling properties of field ionization of Rydberg atoms in single-cycle THz pulses: 1D considerations.** J. Phys. B: At. Mol. Opt. Phys. 49 (2016), 245002 (7pp).

II) M. Chovancova,1 H. Agueny,1 J. J. Rørstad,2 and J. P. Hansen. **Classical and quantum mechanical scaling of ionization from excited hydrogen atoms in single-cycle THz pulses.** Phys. Rev, A 96 (2017), 023423 (10pp).

III) M Chovancova, H Agueny, M Førre, L Kocbach and J P Hansen. **Spatial transport of electron quantum states with strong attosecond pulses.** J. Opt. 19 (2017), 114008 (6pp).

The scientific work displayed in this thesis has been group teamwork all the way. While problem formulation mainly was provided by my supervisor I took part in discussions, programming, analysis and writing

PAPER I

PAPER II

Classical and quantum-mechanical scaling of ionization from excited hydrogen atoms in single-cycle THz pulses

M. Chovancova,[1] H. Agueny,[1] J. J. Rørstad,[2] and J. P. Hansen[1]
[1]*Department of Physics and Technology, Allegt. 55, University of Bergen, N-5007 Bergen, Norway*
[2]*Department of Physics and Astronomy, Aarhus University, 8000 Aarhus C, Denmark*
(Received 19 April 2017; revised manuscript received 12 July 2017; published 25 August 2017)

Excited atoms, or nanotip surfaces, exposed to strong single-cycle terahertz radiation emit electrons with energies strongly dependent on the characteristics of the initial state. Here we consider scaling properties of the ionization probability and electron momenta of H(nd) atoms exposed to a single-cycle pulse of duration 0.5–5 ps, with $n = 9,12,15$. Results from three-dimensional quantum and classical calculations are in good agreement for long pulse lengths, independent of pulse strength. However, differences appear when the two approaches are compared at the most detailed level of density distributions. For the longest pulse lengths a mixed power law, n-scaling relation, $\alpha n^{-4} + (1-\alpha)n^{-3}$ is shown to hold. Our quantum calculations show that the scaling relation puts its imprint on the momentum distribution of the ionized electrons as well: By multiplying the emitted electron momenta of varying initial n level with the appropriate scaling factor the spectra fall onto a common momentum range. Furthermore, the characteristic momenta of emitted electrons from a fixed n level are proportional to the pulse strength of the driving field.

DOI: 10.1103/PhysRevA.96.023423

I. INTRODUCTION

Terahertz (THz) radiation technologies are at present advancing with promising perspectives in a wide range of scientific fields, from fundamental science to real-world applications [1]. Owing to the properties of THz radiation based on low photon energies, the emerging technology has been suggested as a useful source for medical imaging and security [2,3]. In recent years, investigation of single- and half-cycle THz pulses for driving nonlinear phenomena has become possible [4,5], which has exposed new phenomena. For instance, recently, it has been demonstrated experimentally that a strong single-cycle THz pulse applied to excited atoms [6] has led to electron emission with higher energies from tightly bound Rydberg states and with increasing pulse strength. Furthermore, a novel n^{-3} (where n is the quantum number) scaling has been found for the field strength required to attain 10% ionization probability, which later was shown to be valid for arbitrary ionization probability [7]. A similar phenomenon has been discovered for nanosized solid tips exposed to THz pulses: Increasingly narrow tips result in a spectrum of increasingly fast electrons [8]. Studies of the response of solid-state systems to THz radiation is in its infancy. In this context it is relevant to understand the detailed nature of the single atom response to THz radiation in order to separate potential collective phenomena from single atom effects.

On the theoretical side, for single-atom interactions, an empirical scaling relation for 10% ionization probability was put forward by Yang and Robichaux [9], which was shown to be valid for a wide pulse strength and duration range. It gives n^{-4} scaling for pulse durations larger than the classical orbit period of the Rydberg atom (T_n) and a n^2 scaling behavior for short pulses. In that work the quantum calculations are restricted to the initial $n = 15$, $l = 2$ states only while classical trajectory Monte Carlo (CTMC) calculations are the basis of the majority of their work. The dynamics of electron ionization from $n = 15$ levels was further considered in great detail based on time-dependent Schrödinger equation (TDSE) and CTMC calculations in parallel [10]. Here they found excellent agreement between the two approaches and showed that electron emission is strongly favoured along an axis pointing in the opposite direction of the electric polarization vector in the second half-cycle of the pulse. None of these calculations were compared directly with the experimental results of Ref. [6].

In this work we therefore analyze the degree of scaling of the ionization of hydrogen for arbitrary ionization probability from the initial $n = 9,12,15$ d states based on a full three-dimensional (3D) solution of the TDSE and CTMC method. We compare the results for pulses with various strengths and durations. In particular, we compare our results directly with the calculations in [10] and to the experiment in [6]. Furthermore, we explore the characteristics of the emitted electrons for different field ionization. We arrive at three main conclusions and results: First, the 3D quantum calculations, which are in agreement with Ref. [10], support a different scaling than the experimental results of Ref. [6]. Second, even though our CTMC and TDSE results in general agree well at the total probability level, clear discrepancies appear when the two methods are compared at the differential level. In Ref. [10] almost perfect agreement was reported for kinetic emission in the forward or backward direction. Third, we show that application of scaling to the momenta of the emitted electrons puts the spectra on almost the same momentum range. In the next section we describe the applied numerical procedures. Then we present and discuss the main results. Finally, concluding remarks are provided in the last section. Atomic units are used throughout unless otherwise stated.

II. THEORETICAL MODEL

A. TDSE

Within the semiclassical (strong-field) approximation we solve the TDSE,

$$\left[H_e(\vec{r},t) - i\frac{\partial}{\partial t}\right]\psi(\vec{r},t) = 0, \tag{1}$$

where the electronic Hamiltonian contains the field-free Hamiltonian and the time-dependent interaction part given in the length gauge with electric field along the z direction, $\vec{E}(t) = E(t)\vec{e}_z$. To validate the results we first compare with the results in [10] where an exponential expression was used for the electric field,

$$E(t) = -\frac{E_0 C_0 t}{t_w} \exp\left[-\left(\frac{t}{t_w}\right)^2 - 0.1\left(\frac{t}{t_w}\right)^4\right]. \quad (2)$$

Here E_0 is the maximum pulse strength, and C_0, t_w are constants given in [10]. The remaining calculations are performed with a much simpler expression for the electric field,

$$E(t) = \begin{cases} -E_0 \sin(\omega t) & \text{if } -T < t < 0 \\ -E_0 \beta \sin(\beta\omega t) & \text{if } T/\beta > t > 0 \\ 0 & \text{otherwise,} \end{cases} \quad (3)$$

with $\beta \sim 1.5$. This equation grasps the main feature of a single-cycle THz pulse related to the experiments [6,8]; a first positive half-cycle of duration T and a shorter negative and more intense half-cycle of duration T/β. The pulse strength refers to the maximum value of the electric field, i.e., $E_0(n) = E_0\beta$, where n refers to the initial principal quantum number. There are two additional technical advantages of the field expressed by Eq. (3) as well: It can be integrated giving simple analytical expressions for the vector field $A = -\int E(t')dt'$ and the free-field displacement $\alpha = -\int A(t')dt'$. Secondly, the pulse has a well defined start $(-T)$ and end time (T/β). We obtain very similar results for the fields of Eqs. (3) and (2) for $\beta = 1$, but with a factor of 2 shorter simulation time.

Two major numerical challenges with strong THz pulses are related to the long integration times in addition to the required sizes of the numerical grids. Even if techniques have been developed to calculate differential quantities in special situations [11], the full wave function in general needs to be kept on the grid to allow for extraction of all measurable quantities accurately. In the present case at the strongest pulse strength, for example, the wave function initially propagates along the negative z axis and opposite in the final half-cycle. If the grid size is too small, a part of the wave function is absorbed in the first half-cycle and by that the dynamics in the second phase of the field becomes restricted.

The TDSE is integrated using the split-step Fleck-Hermann method [12]. The initial (hydrogen) Rydberg states considered throughout the investigation are analytically known. When put on the grid they are completely stable in absence of electric fields. Here, we need only to consider states with the $m = 0$ component of the magnetic quantum number due to the field polarization. The time-dependent wave function is then expanded in spherical harmonics in the θ and r coordinates as

$$\Psi(r_i,\theta_j,t) = \sum_{l=0}^{L_{\max}} f_l(r_i,t) Y_{l,0}(\hat{r}_j), \quad (4)$$

where $\hat{r}_j = \theta_j$. For general polarizations the sum runs over m-quantum numbers as well and the present formalism is perfectly valid in that case [13]. Then $\hat{r}$ describes the two spherical angles, $d\hat{r}$ describes integration over both and we keep this more general notation in the following. We track the wave function up to radii up to $r_{\max}$ from where an absorbing mask prohibits reflections. Numerical parameters applied $(r_{\max}, \Delta r, L_{\max}, \Delta t)$ are given in the figure captions. Once the time-dependent wave function is determined, on a sufficiently large grid containing the entire density, the wave function in momentum space is calculated using the same basis of spherical harmonics as in Eq. (4). We define the Fourier transform

$$\langle p|\Psi\rangle = \tilde{\Psi}(\vec{p},t) = \int d^3r\, e^{-i\vec{p}\cdot\vec{r}} \Psi(\vec{r},t) \quad (5)$$

and the plane wave expansion

$$e^{i\vec{p}\cdot\vec{r}} = 4\pi \sum_{L,M=0}^{\infty} i^L j_L(pr) Y^*_{L,M}(\hat{r}) Y_{L,M}(\hat{p}). \quad (6)$$

Here $\hat{r}, \hat{p}$ denotes the spherical angles and $j_L(x)$ is defined by the spherical Bessel function, $J_n(x)$, $j_l(x) = \frac{1}{\sqrt{x}} J_{l+0.5}(x)$. Inserting this expansion into the Fourier transform we find that the radial expansion of Eq. (4) can be expressed in momentum space as

$$\tilde{\Psi}(\vec{p},t) = \sum_{l=0}^{L_{\max}} \tilde{f}_l(p,t) Y_{l,0}(\hat{p}). \quad (7)$$

After the pulse, the continuum part of $\tilde{\Psi}$ spans the basis describing ionization, $\tilde{\Psi}^c(\vec{r},t) = \tilde{\Psi} - \tilde{\Psi}^{\text{bound}}$,

$$\tilde{\Psi}^c(\vec{p},t) = \sum_{l=0}^{L_{\max}} \tilde{f}^c_l(p,t_f) Y_{l,0}(\hat{p}). \quad (8)$$

The momentum functions $\tilde{f}^c_l$ become the Fourier transform of the continuum part of the radial functions. These are obtained by projecting and subtracting all populated hydrogenic bound states at t_f. The differential scattering cross section for emission of an electron with momentum $|p_n|$, integrated over angles, can now be calculated from $\tilde{\Psi}^c$,

$$\frac{d\sigma}{dp_n} = \int d\hat{p}\, p^2 |\langle p|\Psi(\vec{r},t_f)\rangle|^2 = \sum_{l=0}^{L_{\max}} \left|p_n \tilde{f}^c_l(p_n,t_f)\right|^2. \quad (9)$$

The angular resolved cross section requires additional multiplication of phases connected to the long-range property of the Coulomb potential. To achieve the correct expression it is convenient to start from a conventional basis state expansion of the time-dependent wave function,

$$\Psi(\vec{r},t_f) = \sum_m a_m(t_f)\Phi_m(\vec{r}) + \sum_n b_n(t_f)\Phi^c_n(\vec{r}). \quad (10)$$

Here, the sum over $m(n)$ runs over all bound (discretized continuum) states inside a sphere with radius $r_{\max}$. The basis functions are the product of radial and angular states, $\Phi_k(\vec{r}) = \phi_k(r)Y_{l,0}(\hat{r})$, and the grid is assumed to span the entire wave function after the pulse, $1 = \sum_m |a_m(t_f)|^2 + \sum_n |b_n(t_f)|^2$. The connection between the set Ψ_n and the correct outgoing scattering states of the Coulomb problem is obtained when expressing the latter in terms of the discretized basis defined

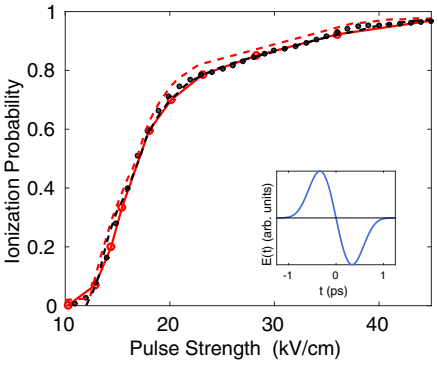

FIG. 1. Ionization probabilities as a function of pulse strength for the symmetric pulse, Eq. (2), sketched in the inset and applied in [10]. The black dashed line is the TDSE results and the dots are the CTMC results from [10]. The red (dark-gray) bulleted curve displays the present TDSE results and the red (dark-gray) dashed line the CTMC results. Parameters for the TDSE computations: $r_{\max} = 4000$, $\Delta r = 0.2441$, $L_{\max} = 128$, $\Delta t = 0.05$ and pulse parameters: $t_w = 2.067\,069 \times 10^4$, $C_0 = 2.385\,525\,5$.

above,

$$\Psi_C(\vec{r}) = \frac{1}{p}\sum_{l=0}^{\infty}\sum_{n} i^l e^{i\delta_l}\phi^c_{n,l}(r;p_n)Y^*_{l,0}(\hat{p})Y_{l,0}(\hat{r}), \qquad (11)$$

where the Coulomb phase shift is $\delta_l = \arg[\Gamma(l+1+i/p)]$ [14]. The projection of the numerical basis of Eq. (10) then becomes

$$\langle\Psi_C|\Psi\rangle = \frac{1}{p}\sum_{l=0}^{L_{\max}}\sum_{n}(-i)^l e^{-i\delta_l} b_n(t_f)Y_{l,0}(\hat{p}). \qquad (12)$$

The differential angular cross section for emission of an electron with any energy in the direction $d\hat{p}$ then becomes

$$\frac{d\sigma}{d\hat{p}} = \int dp\, p^2 |\langle\Psi_C|\Psi\rangle|^2 = \sum_n \left|\sum_{l=0}^{L_{\max}}(-i)^l e^{-i\delta_l} b_n(t_f)Y_{l,0}(\hat{p})\right|^2. \qquad (13)$$

Note that amplitudes of the numerical simulation have to be augmented by the Coulombic phase factors before integration. The same procedure must be carried through for the grid expansion of Eq. (4). Starting again with the projection on the Coulomb functions,

$$\langle\Psi_C|\Psi\rangle = \int d^3r \langle\tilde{\Psi}_C|\vec{r}\rangle\langle\vec{r}|\Psi\rangle = \sum_{l=0}^{L_{\max}}(-i)^l e^{-i\delta_l}\tilde{f}^C_l(p)Y_{l,0}(\hat{p}). \qquad (14)$$

By comparing this expression with Eq. (8) we identify $\tilde{f}^C_l(p) = \tilde{f}^c_l(p)$ and we note that Coulomb phase shifts need to be augmented precisely as in the case of eigenstate expansions, Eqs. (13) and (12). The differential cross sections for emission of an electron with momentum p_n along the direction $d\hat{p}$ then

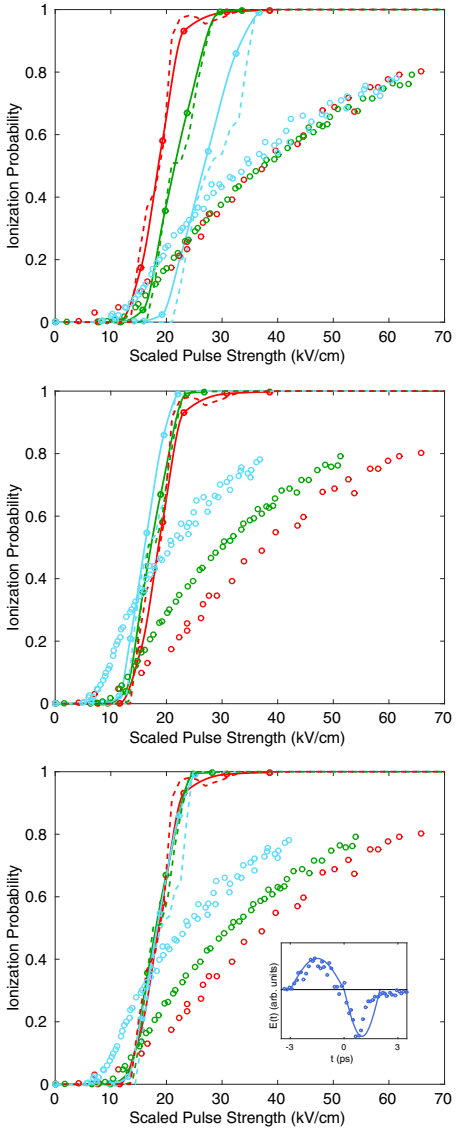

FIG. 2. Ionization probabilities as a function of scaled pulse strength for a pulse shape comparable to the experiment of [6] (cf. inset in the lower panel). Pulse parameters from Eq. (3) are $T = 124\,020$ a.u. ($\omega = 2.533\,13 \times 10^{-5}$ a.u.), $\beta = 1.5$. Probabilities are shown as a function of scaled pulse strength. The upper (middle) panel shows the experimental and computational results based on a n^{-3} (n^{-4}) scaling. The lower panel shows the results for the mixed scaling Eq. (20), with $\alpha = 0.2$. Color coding is according to the initial n state with $n = 15$ as red (dark-gray) lines, $n = 12$ as green (gray) lines, and $n = 9$ as blue (light-gray) lines. Full curves are TDSE results, broken curves are CTMC results, and bullets are experimental data from [6] with the same color coding. Parameters of the TDSE computations: $r_{\max} = 4000$, $\Delta r = 0.2441$, $L_{\max} = 128$, $\Delta t = 0.05$.

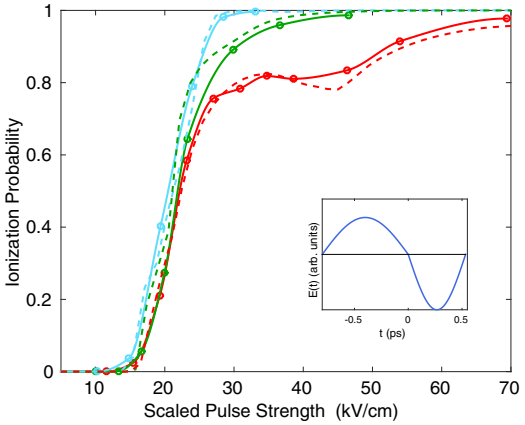

FIG. 3. Ionization probabilities as a function of scaled pulse strength for a pulse shape of Eq. (3), comparable in length to the pulse in Fig. 1. Results are plotted in terms of the mixed scaling Eq. (20), with $\alpha = 0.2$. Pulse parameters are $T = 33\,073.0$ a.u. ($\omega = 9.498\,96 \times 10^{-5}$ a.u.), $\beta = 1.5$. Color coding is according to the initial n state with $n = 15$ as red (dark-gray) lines, $n = 12$ as green (gray) lines, and $n = 9$ as blue (light-gray) lines and full curves are TDSE results. Parameters of the TDSE computations: $r_{\max} = 4000$, $\Delta r = 0.2441$, $L_{\max} = 128$, $\Delta t = 0.05$.

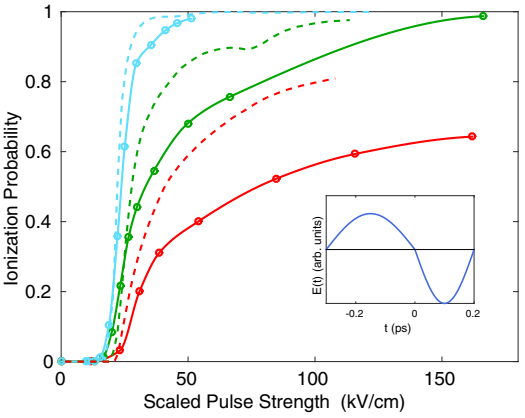

FIG. 4. Ionization probabilities as a function of scaled pulse strength, Eq. (20), for a pulse shape of Eq. (3), with duration only 10% of the pulse in Fig. 2, $T = 12\,402.0$ a.u. ($\omega = 2.533\,13 \times 10^{-4}$ a.u.), $\beta = 1.5$. Color coding is according to the initial n state with $n = 15$ as red (dark-gray) lines, $n = 12$ as green (gray) lines, and $n = 9$ as blue (light-gray) lines and full curves are TDSE results. Parameters of the TDSE computations: $r_{\max} = 4000$, $\Delta r = 0.2441$, $L_{\max} = 128$, $\Delta t = 0.05$.

becomes

$$\frac{d\sigma}{dp_n d\hat{p}} = p_n^2 |\langle \Psi_C | \Psi \rangle|^2 = \left| \sum_{l=0}^{L_{\max}} (-i)^l e^{-i\delta_l} p_n \tilde{f}_l^c(p_n, t_f) Y_{l,0}(\hat{p}) \right|^2 . \quad (15)$$

Thus, the differential cross sections can be computed directly based on the available radial (momentum) basis $f_l^c(r)$ [$\tilde{f}_l^c(p)$] without explicit knowledge of the continuum basis function ϕ_n of Eq. (12). For ionization from the $n = 15$ initial state the final lowest electron momenta are relatively small, in fact of similar magnitude as the strength of the potential energy. Therefore the quantum angular scattering can be affected by the Coulomb phase shifts as well. The differential cross section for electron emission in the forward direction is obtained by integrating over angles corresponding to a positive [$\theta \in (0, \pi/2)$] or negative [$\theta \in (\pi/2, \pi]$] p_z momentum component,

$$\frac{dP^{\text{forward}}}{dp_n} = \int_0^{\pi/2} \int_0^{2\pi} d\hat{p} \frac{d\sigma}{dp_n d\hat{p}}, \qquad \frac{dP^{\text{backward}}}{dp_n} = \int_{\pi/2}^{\pi} \int_0^{2\pi} d\hat{p} \frac{d\sigma}{dp_n d\hat{p}}. \quad (16)$$

These quantities will be discussed at the end of the next section and compared with (phase-free) classical scattering.

B. CTMC

In the CTMC method, Newton's equations are propagated for a large number of the initial conditions describing some main characteristics of an initial quantum probability density. This approach has been applied for decades within heavy particle collisions [15,16] before it was adopted in the study of atoms interacting with strong laser fields [17,18]. A variety of possibilities exist to select the initial distributions [19]. When ionization via tunneling is important an initial distribution of the initial electron position and momenta after tunneling is useful [20]. After propagating the electron positions and momenta according to a given time-dependent interaction, quantum phases may even be added in the final statistics [21].

The basic (standard) CTMC method which we will apply here is based on the selection of initial states which have a fixed energy identical to the initial quantum state in question. The simplest assumption that otherwise the probability density is a constant D is then in N-dimensional space,

$$D d^N r d^N p \delta[E(\vec{r}, \vec{p}) - E_0]. \quad (17)$$

This is referred to as the microcanonical distribution [22], which is based on the formal similarity with the concept of the microcanonical ensemble in statistical physics. There is no proof that this method should model well the quantum probability densities and the field-induced dynamics other than the results. And indeed, fine details related to differential quantities often display discrepancies with full quantum treatments [17,23].

In this approach the energy delta function limits the $2N$-dimensional space to $2N - 1$ dimensions, with the necessity to find the $2N - 1$ uniformly distributed variables. In 3D ($N = 3$) space with two sets of spherical coordinates, the four angles are treated in the standard way of covering uniformly the two spheres in r and p. The remaining radial r and p must be described by only one uniformly distributed variable usually denoted w. This is obtained by transforming $p^2 dp r^2 dr \longrightarrow dE dw$ and $pdp \rightarrow \mu dE$ so that the energy delta function can

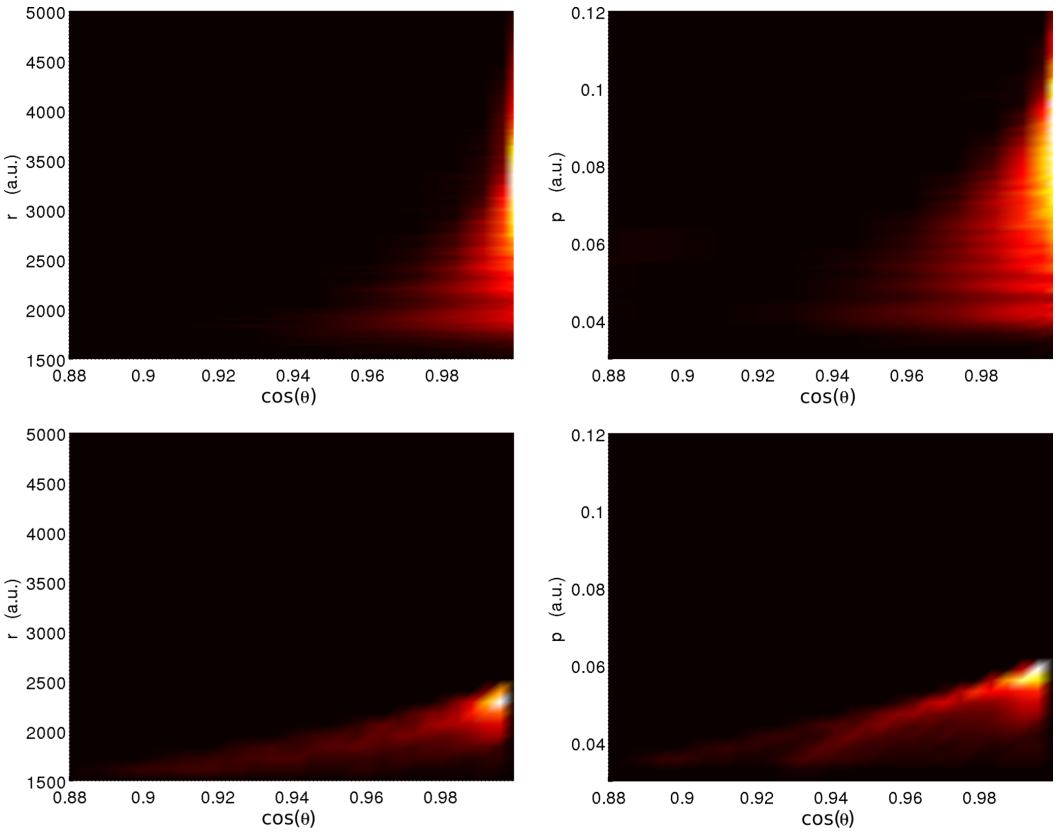

FIG. 5. Probability density distributions at the end of the pulse of the continuum part of the quantum wave function in position space, $|\Psi^c[r, \cos(\theta), t_f]|^2$ (upper left) and momentum space $|\tilde{\Psi}^c[p, \cos(\theta_p), t_f]|^2$ (upper right) for an initial $15d$ state with a pulse strength corresponding to 20% ionization probability ($E_0 = 18$ kV/cm) in Fig. 3. The lower panels show the corresponding densities from CTMC calculations. Pulse parameters from Eq. (3) are as in Fig. 2: $T = 124\,020$ a.u. ($\omega = 2.533\,13 \times 10^{-5}$ a.u.), $\beta = 1.5$. Parameters of the TDSE computations: $r_{\max} = 16\,000$, $\Delta r = 0.2441$, $L_{\max} = 128$, $\Delta t = 0.05$.

be integrated over dE. The variable w can then be found from these requirements.

$$w(r) = \mu \int_0^r p(r')^{\prime 2} dr' = \mu \int_0^r \sqrt{2\mu[E_0 - V(r')]}\, r'^2 dr'. \tag{18}$$

In this equation E_0 is the fixed initial energy and μ is the reduced mass. For more details, see Ref. [22].

In addition, to mimicking the initial $Y_{l=2,m=0}$ character of the quantum initial state, we select only classical initial conditions with angular momentum l, $1.5 < l < 2.5$, and $|l_z| < 0.5$. No sensitivity on the results to other limits for $l \sim 2$, $l_z \sim 0$ is found. Newton's equations are then propagated with up to 500 000 initial states using the adaptive integration method of Shampine and Gordon [24] and carefully checked by the ODE45 routine in MATLAB. In both cases an absolute (relative) error tolerance below 10^{-7} (10^{-9}) has been applied.

III. RESULTS AND DISCUSSION

In the remainder of this paper, scaling laws will be discussed in connection with the ionization probabilities and their momentum distributions from TDSE and CTMC calculations. The angular distributions, which show distinct differences, will be additionally discussed at the end.

We start out by comparing the results of our methods with the results of Ref. [10]. Here, we restrict ourselves to the ionization probabilities as a function of the peak field for the hydrogen $15d$ state, but test calculations with the initial $15s$ show the same degree of agreement. The quantum probabilities are computed by subtracting from unity all bound-state probabilities pertaining to a sphere of a given radius (see Fig. 1 caption). The classical probabilities are obtained by the fraction of final states with positive energy after the pulse and the results from both approaches are plotted in Fig. 1. In the same figure the quantum and classical probabilities of [10] are shown. Results are shown for a

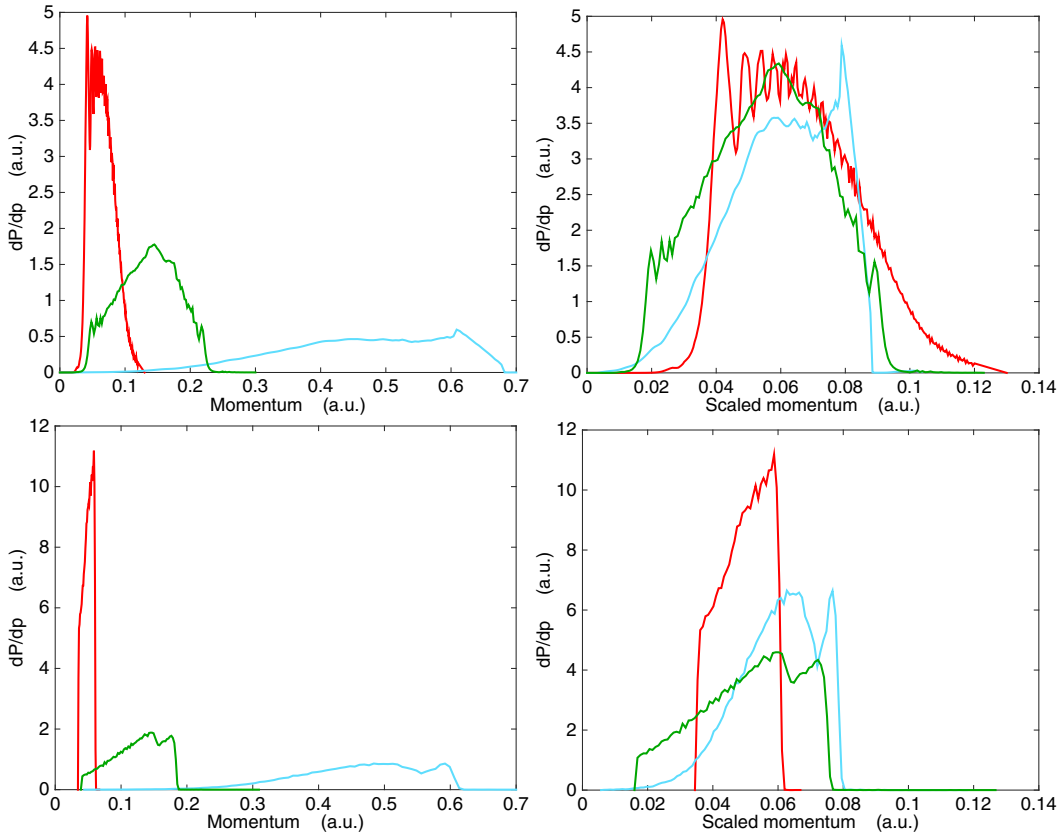

FIG. 6. Momentum distributions of the ionized electron based on the TDSE approach (upper) Eq. (9) and CTMC (lower), for initial states nd with $n = 15$ as red curves (dark-gray), $n = 12$ as green curves (gray), and $n = 9$ as blue (light-gray) curves and for pulse strengths leading to 20% ionization probability from each initial n state ($E_0 = 18$ kV/cm for initial $n = 15$, $E_0 = 36$ kV/cm for initial $n = 12$, $E_0 = 104$ kV/cm for initial $n = 9$). The right column shows the same distributions except that the $n = 12$ and $n = 9$ momentum distributions have been scaled according to the mixed scaling relation, Eq. (20), with $\alpha = 0.2$. Pulse parameters from Eq. (3) are as in Fig. 2: $T = 124\,020$ a.u. ($\omega = 2.533\,13 \times 10^{-5}$ a.u.), $\beta = 1.5$. Parameters of the TDSE computations: $r_{\max} = 16\,000$ ($r_{\max} = 32\,000$ for $n = 9$), $\Delta r = 0.2441$, $L_{\max} = 128$, $\Delta t = 0.05$. The CTMC results are based on 500 000 initial states.

symmetric pulse with a duration of $\sim$2 ps, and its form is illustrated in the inset of the Fig. 1. One can see that the present computed TDSEs are in excellent agreement with those reported in Ref. [10]. Our classical calculations (red dashed lines) very slightly overestimate the ones obtained in [10], possibly a result of different strategies to sample the initial conditions.

In [9] an empirical scaling law was shown to be valid for total ionization (at 10% ionization probability) for a large parameter range of initial states, pulse lengths, and strengths. This was based predominantly on classical calculations but included also results from a few quantum calculations. This scaling law implies a n^2 scaling behavior for pulse durations shorter than the classical orbit period of the Rydberg atom ($T_n \sim n^3$). At long pulse lengths, their scaling law reproduces the results of the classical over the barrier model, i.e., a n^{-4} scaling. In the transition region between these two extrema any kind of power/nonpower laws may occur, including the measured and reported n^{-3} scaling in [6].

Instead of testing scaling law in [9] for computations with different initial levels and probabilities, we here aim to investigate the possible degree of scaling at all ionization probabilities for selected single-cycle pulses. We will consider pulse lengths comparable to the $n = 15$ orbit time of $\sim$0.5 fs, and upward to $\sim$5 fs, the experimental pulse length in [6]. In Fig. 2 we compare our calculated results with the experimental results directly and for various forms of scaling. In the upper panel the experimental ionization probabilities of the initial $n = 9, 12, 15$ states are shown on a common scaled axis defined by $(n/15)^3$ [7]. We observe that this scaling is excellent for the experimental results but rather poor for the calculations. On the other hand, TDSE and CTMC probabilities are in

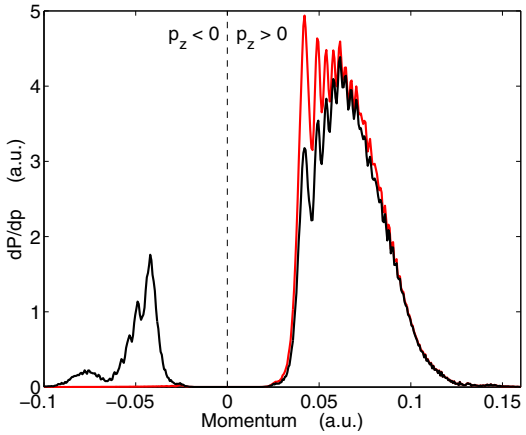

FIG. 7. Forward and backward quantum differential momentum emission probability (black curve) for the initial state $n = 15d$, $E_0 = 18$ kV/cm, Eq. (16), and compared to the momentum distribution of Eq. (9), the red (dark-gray) curve shown in Fig. 6. Parameters of the TDSE computations: $r_{\max} = 16\,000$, $\Delta r = 0.2441$, $L_{\max} = 128$, $\Delta t = 0.05$.

good agreement. The situation switches by applying over the barrier scaling, $(n/15)^4$ in the middle panel of Fig. 2. Now the calculations shows a higher degree of scaling while the scaling of the experimental results are poor.

A dynamical classical mechanism behind the observed n^{-3} scaling was put forward in Ref. [6]. Interestingly, a one-dimensional quantum tunneling mechanism provides the same power-law dependence independent of field strength [25]. In 3D, the weak-field adiabatic tunneling theory provides a leading exponential term which partly scales as n^{-3} as well [26]. Thus, tunneling offers a quantum-mechanical mechanism leading to the observed scaling. The strong external field does, however, open for over the barrier ionization as well. When the two processes takes place at the same time a combination of n^{-3} and n^{-4} scaling may show up in the results. A mixed power-law scaling factor would then emerge on the form

$$E_0^{sf}(n) = \alpha n^{-4} + (1-\alpha)n^{-3}, \tag{19}$$

where the parameter $0 \geqslant \alpha \leqslant 1$. Given an ionization probability for a reference n level, say $n = 15$, the scaled pulse strength of ionization from other n levels at a given real pulse strength $E_0(n)$ becomes

$$E_0^{\text{scaled}}(n) = \frac{E_0^{sf}(n)}{E_0^{sf}(n=15)} E_0(n). \tag{20}$$

If the present scaling is universally valid the ionization probability for varying initial n levels falls on the same curve for a fixed value of the parameter α. In the lower panel of Fig. 2 it is interesting to observe that the computed quantum ionization probabilities exhibit this property for $\alpha = 0.2$. Even the CTMC calculations display the same scaling property for ionization probabilities below 50%. However, putting the experimental results through this scaling procedure only slightly improves the situation from the middle panel of Fig. 2. A potential origin of the discrepancy might be related to the fact that the experiment is performed with Na atoms and the calculations are with H atom(s). However, the quantum defects of the initial nd states in Na are very small and a complete change of scaling is hardly expected between the two atomic systems [9]. Given the agreement with independent calculations we can only conclude that we here document an unresolved discrepancy between theory and experiment which calls for an iteration or independent work on the experimental and possibly also on the computational side.

In Fig. 3 we show our results for a shorter pulse length than the one in Fig. 2, and comparable to the one in Fig. 1. In relation to Fig. 2 the time-dependent field now has a stronger (negative) pulse strength in the second half-cycle as compared to the first. We again note a sharp rise in the ionization probability at the same pulse strength range as in Figs. 1 and 2 and that the scaling procedure as outlined above works very well up to an ionization probability around 70%. At that point the $n = 15$ ionization probability flattens out and oscillates, a mechanism discussed in [6]. It occurs when the pulse length becomes comparable to the classical orbit time, $T_n \propto n^3$. The results of a much shorter pulse duration ($\sim$0.5 ps) are shown in Fig. 4. At this point the scaling procedure is only valid at smallest ionization probabilities. At ionization probabilities exceeding 10% the results of classical and quantum calculations disagree. This indicates that the empirical scaling relation put forward in [9] is limited to small ionization probabilities only.

In the remaining part of this section we will study the momentum distributions in more detail. It generally requires much more computationally expensive calculations as the entire wave function needs to be kept on the grid until the electric field vanishes. The momentum and angular distributions indeed provide a deeper understanding of the ionization dynamics. In this context, it was found in the recent experiment [6], by measuring the electron energy distributions for different n states, that lower initial n gives generally higher energies of the emitted electrons. We address here two main questions: First, to which degree does the mixed scaling law of Eq. (19) imprint itself on the spectrum of emitted electrons? Second, to which extent do the CTMC and TDSE calculations agree when the differential distribution is studied in detail?

The starting point amounts to examining the ionization dynamics in the two-dimensional position and momentum spaces at the end of the laser pulse. Figure 5 shows the spatial distribution of the continuum part of the electron-probability density (left panels) and the corresponding momentum distribution (right panels) for the initial $15d$ state at 20% ionization probability (see caption for further details). The distributions are quantum (upper panels) and classical (lower panels) and they are seen to display great differences. The spreading, the mean position, and momentum of the outgoing distribution differ. With a less detailed focus there are also common features: It is seen that the electron density which is nonzero along a limited range of $(r, \cos\theta)$ values corresponds to ionized electrons propagating along the positive z axis and are centered at positive z values immediately after the pulse. This is consistent with the ionization dynamics taking part predominantly in the final half-cycle of the pulse. In the quantum results, we also observe the emergence of oscillatory

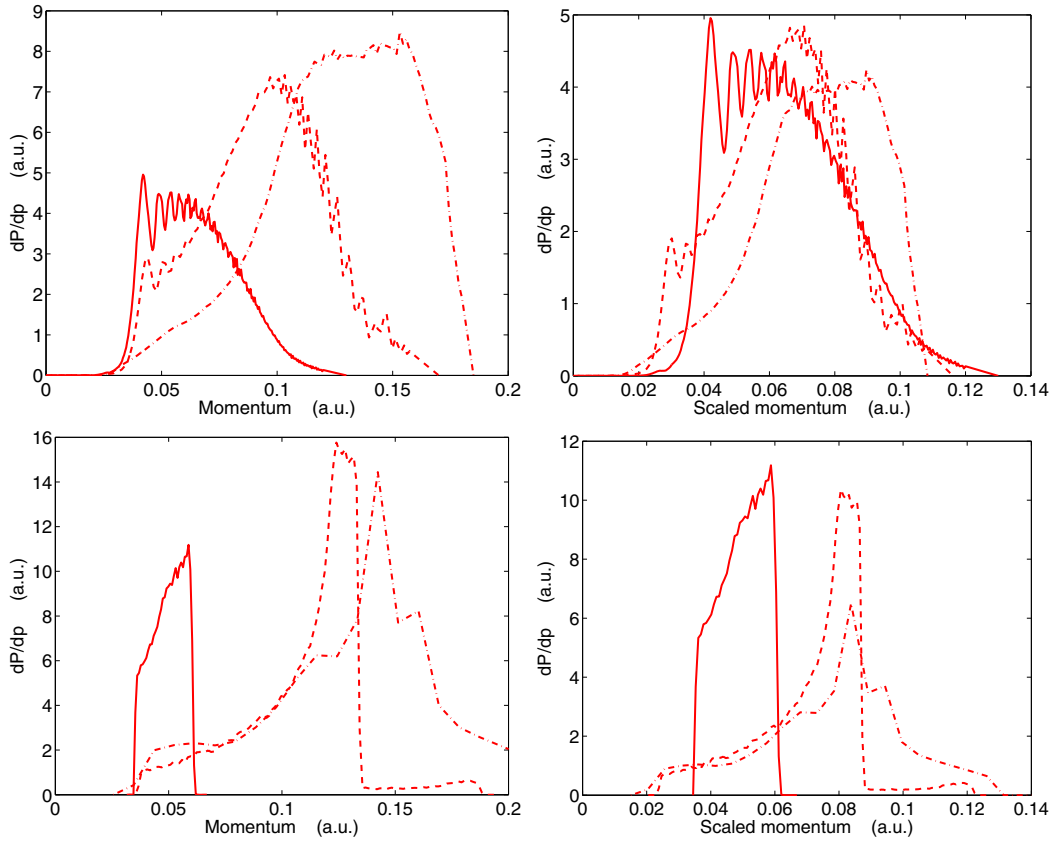

FIG. 8. Upper panels: Momentum distributions from the initial $n = 15d$ state for for three different pulse strengths $E_0 = 15.8$ kV/cm (full line), $E_0 = 18.5$ kV/cm (dashed line), and $E_0 = 21.6$ kV/cm (dashed-dotted line). Pulse parameters from Eq. (3) are as in Fig. 2: $T = 124\,020$ a.u. ($\omega = 2.533\,13 \times 10^{-5}$ a.u.), $\beta = 1.5$. The pulse strengths give ionization probabilities of 20%, 50%, and 73% for the TDSE calculations. The upper right panel shows the distribution with a linearly scaled momenta [cf. Eq. (22)] and normalized to an ionization probability of 20%. Lower panels: Corresponding spectra based on CTMC calculations with 500 000 initial states. Parameters of the TDSE computations: $r_{\max} = 16\,000$, $\Delta r = 0.2441$, $L_{\max} = 128$, $\Delta t = 0.05$.

wavelike structures which do not appear in classical results. A related phenomenon has been discussed previously in Refs. [27] in a multicycle extreme-ultraviolet pulse, and in studies of strong-field few-cycle ionization of the ground state about 20 years ago [17,28].

We turn now to discuss the scaling properties in connection with the momentum distributions of the ionized electrons. In Fig. 6 we have integrated the distributions over all angles and obtained the differential momentum distribution, dP/dp. In the left panel of Fig. 6 we show the unscaled quantum (upper panels) and classical (lower panels) distributions for three initial $n = 9, 12, 15$ states all at $\sim 20\%$ ionization probability. The general features of quantum distributions are reflected in the classical distributions. These are mainly manifested by a wider distribution describing higher electron momenta for decreasing n. By applying the mixed scaling relation, Eq. (19), to the final state momenta, one can now see that the quantum distributions of all three initial states fall into a common range. To some extent the classical distributions also exhibit this property, but here the scaled range is "less common," as shown in the right column of Fig. 6. This result is consistent with the release of the electron at a narrow range of critical pulse strengths, from which it essentially propagates with little influence of the binding potential, as discussed in [7,9].

The instantaneous CTMC distribution of Fig. 6 does not change at all by letting the particles propagate an additionally long time in the presence of the Coulumb potential only. For the quantum distribution it is not so: The low-energy part of the continuum waves, in particular, may be altered by the Coulomb potential. Thus Coulomb phases need to to be added when computing the final differential forward or backward emission probability [cf. Eq. (15)]. This is displayed in Fig. 7 for the initial $n = 15d$ results in Figs. 5 and 6. We observe

that indeed the Coulomb potential plays a role and causes the low-energy part of the emitted spectrum to be rescattered in the opposite direction from what is seen in Fig. 5. Thus, the forward-backward scattering asymmetry turns out to be different for TDSE and CTMC calculations as well, notably in disagreement with the results in [10] with other pulse shapes, strengths, and durations.

For completeness, we address in Fig. 8 the nature of the momentum distributions for an initial fixed n level and for different ionization probabilities. The left panel of Fig. 8 shows results at three comparable ionization probabilities for the initial $n = 15d$. Both the quantum distribution (upper panels) and the classical one (lower panels) show increasing momenta with increasing pulse strength. But again, the detailed distribution differs in shape. A possible scaling in this case can be argued for by assuming the ratio between the final momenta and the pulse strength of any ionization probability, $x\%$, is almost constant,

$$\frac{p(20\%)}{E_0(20\%)} = \frac{p(x\%)}{E_0(x\%)}. \tag{21}$$

This suggests a scaling relation of the form

$$p^{\text{scaled}}(x\%) = \gamma \frac{E_0(20\%)}{E_0(x\%)} p(x\%) \tag{22}$$

with $\gamma \sim 1$ as a free fitting parameter may work. The spectra are additionally normalized to the same total area. We observe in Fig. 8 (right panel) that the momentum range of emitted electrons from the quantum results scale reasonably well for $\gamma = 0.8$, while the CTMC results differ much more, both in shape and final scaled momentum range.

IV. CONCLUDING REMARKS

We have considered the response of H($n = 9d, 12d, 15d$) atoms to a single-cycle THz pulse with durations from 0.5 to 5 ps in classical and quantum-mechanical time propagation. A scaling law has been found to be generally valid for any ionization probability and for initial $n = 9, 12, 15$ levels when the pulse length becomes similar to, or longer than, the classical period of the n levels under consideration. We further investigated the scaling behavior in connection with the ionized momentum distribution in the long-pulse regime. The same scaling property was here found to be valid in quantum distributions and to a much lesser degree for the classical approach. The Coulomb phases have been shown to be important in the quantum scattering process as well for the initial $n = 15d$ state. Finally, a near linear response of the characteristic momentum range has been found for ionization from a fixed n state with increasing pulse strength.

Interestingly, these phenomena have a counterpart in THz radiation from nanotips, faster electrons from narrower tips, and a linear response for a fixed tip with increased pulse strength [8]. Further investigations in this direction may lead to new imaging devices where the electron spectrum from a fixed pulse may provide structural information of the tip region itself. Before that it seems important to further investigate the scaling relations validity for single atoms in strong THz fields. This applies to electron emission probabilities at the total as well as at the differential level and to converge on parameter ranges where ionization and scattering from classical and quantum based approaches agree.

ACKNOWLEDGMENTS

The research has been supported by UNINETT Sigma2 AS which manages the national infrastructure for computational science in Norway. Numerical calculations were carried out at the Cray XE6 (Hexagon) supercomputer installation at Parallab at the University of Bergen (UiB).

[1] S. S. Dhillon *et al.*, J. Phys. D: Appl. Phys. **50**, 043001 (2017).
[2] M. Tonouchi, Nat. Photon. **1**, 97 (2007).
[3] J. F. Federici, B. Schulkin, F. Huang, D. Gary, R. Barat, F. Oliveira, and D. Zimdars, Semicond. Sci. Technol. **20**, S266 (2005).
[4] J. L. LaRue, T. Katayama, A. Lindenberg, A. S. Fisher, H. Öström, A. Nilsson, and H. Ogasawara, Phys. Rev. Lett. **115**, 036103 (2015).
[5] K. Kovács, E. Balogh, J. Hebling, V. Tosa, and K. Varjú, Phys. Rev. Lett. **108**, 193903 (2012).
[6] S. Li and R. R. Jones, Phys. Rev. Lett. **112**, 143006 (2014).
[7] H. Agueny, M. Chovancova, J. P. Hansen, and L. Kocbach, J. Phys. B: At., Mol. Opt. Phys. **49**, 245002 (2016).
[8] S. Li and R. R. Jones, Nat. Commun. **7**, 13405 (2016).
[9] B. C. Yang and F. Robicheaux, Phys. Rev. A **90**, 063413 (2014).
[10] B. C. Yang and F. Robicheaux, Phys. Rev. A **91**, 043407 (2015).
[11] L. Tao and A. Scrinzi, New J. Phys. **14**, 013021 (2012).
[12] M. R. Hermann and J. A. Fleck, Jr., Phys. Rev. A **38**, 6000 (1988).
[13] J. P. Hansen, T. Sørevik, and L. B. Madsen, Phys. Rev. A **68**, 031401(R) (2003).
[14] P. G. Burke, *R-Matrix Therory of Atomic Collisions* (Springer Verlag, Berlin, 2011).
[15] N. C. Blais and D. L. Bunker, J. Chem. Phys. **37**, 2713 (1962).
[16] R. Abrines and I. C. Percival, Proc. Phys. Soc. **88**, 861 (1966).
[17] J. P. Hansen, J. Lu, L. B. Madsen, and H. M. Nilsen, Phys. Rev. A **64**, 033418 (2001).
[18] J. S. Cohen, Phys. Rev. A **64**, 043412 (2001).
[19] N. D. Cariatore, S. Otranto, and R. E. Olson, Phys. Rev. A **93**, 066702 (2016).
[20] J.-P. Wang and F. He, Phys. Rev. A **95**, 043420 (2017).
[21] E. A. Solov'ev, Eur. Phys. J. D **65**, 331 (2011).
[22] C. O. Reinhold and C. A. Falcón, Phys. Rev. A **33**, 3859 (1986).

[23] A. Dubois and J. P. Hansen, J. Phys. B: At., Mol. Opt. Phys. **29**, L225 (1996).
[24] L. F. Shampine and M. K. Gordon, *Computer Solution of Ordinary Differential Equations: The Initial Value Problem* (Freeman, San Fransisco, 1975).
[25] R. G. Forbes, J. Appl. Phys. **103**, 114911 (2008).
[26] T. Yamabe, A. Tachibana, and H. J. Silverstone, Phys. Rev. A **16**, 877 (1977).
[27] I. A. Ivanov, A. S. Kheifets, K. Bartschat, J. Emmons, S. M. Buczek, E. V. Gryzlova, and A. N. Grum-Grzhimailo, Phys. Rev. A **90**, 043401 (2014).
[28] E. Cormier and P. Lambropoulos, Eur. Phys. J. D **2**, 15 (1998).

PAPER III

Appendices

Atomic Units

Through the thesis Hartree atomic units (a. u.) have been used unless stated otherwise. In this set of units the electronic mass, the elementary charge, the angular momentum and the electrostatic constant are all scaled to unity: $m_e = e = \hbar = 4\pi\varepsilon_0 = 1$.

Fundamental and derived Hartree atomic units

Quantity	Unit	Physical significance	Value in SI-units
Mass	m_e	Electron mass	$9.109\,38 \times 10^{-31}$ kg
Charge	e	Absolute value of electron charge	$1.602\,18 \times 10^{-19}$ C
Angular momentum	$\hbar$	Planck constant divided by 2π	$1.054\,57 \times 10^{-34}$ kg
Electrostatic constant	$4\pi\varepsilon_0$	4π times the permitivity of free space	$1.112\,65 \times 10^{-10}$ Fm^{-1}
Length	$a_0 = \frac{\hbar}{m_e c\alpha}$	Bohr radius of atomic hydrogen	$5.291\,77 \times 10^{-11}$ m
Velocity	$v_0 = \alpha c$	Magnitude of electron velocity in first orbit	$2.187\,69 \times 10^{6}$ ms^{-1}
Energy	$E_h = \alpha^2 m_e c^2$	Twice of binding energy of atomic hydrogen	4.35975×10^{-18} J = 27.2114 eV
Frequency	$f = \frac{v_0}{2\pi a_0}$	Angular frequency of electron in first Bohr orbit divided by 2π	$6.579\,69 \times 10^{15}$ s^{-1}
Electric field strength	$F_0 = \frac{e}{(4\pi\varepsilon_0)a_0^2}$	Strength of the Coulomb field experienced by an electron in the first Bohr orbit of atomic hydrogen	$5.142\,21 \times 10^{11}$ Vm^{-1}

Here $\alpha = e^2/(4\pi\varepsilon_0\hbar c) \sim 1/137$ is the fine structure constant.
Hartree atomic units should not be confused with Rydberg atomic units, which are based on slightly different scaling assumptions: $4\pi\varepsilon_0 = 1$, $m_e = 1/2$, $\hbar = 1$ and $e = 1/\sqrt{2}$. Consequently the unit of energy in the two systems differs by a factor of two, i.e., $E_H = 2E_{Ry}$.

Derivation of Quantum Scattering Formulae

A one-electron wavefunction $\Psi(\mathbf{r})$ which has been exposed to a time-dependent from (t_i, t_f) field may be partly of fully excited or ionized. It takes the following form at t_f,

$$\Psi(\mathbf{r}, t_f) = \sum_m a_m(t_f)\Phi_m(\mathbf{r}) + \sum_n f_{i,n}(\Omega, t_f)\frac{e^{ip_n r}}{r} \tag{1}$$

The first part is a sum over bound states while the second is an outgoing wave with $f_{i,n}$ being the scattering amplitude for scattering into a solid angle element Ω_n of the outgoing wave vector when initially the wavefunction is in the state $\Phi_i(\mathbf{r})$. At $t > t_f$ $|a_m|, |f_{i,n}|$ does not depend on time. The differential cross section is,

$$\frac{d\sigma}{p^2 dp d\Omega} = |f_{i,n}(\Omega, t_f)|^2 \tag{2}$$

which is the relative (differential) flux of momentum in a direction perpendicular through the solid angle element Ω. When using the result of a numerical solution of the TDSE as a starting point for differential fluxes it is implicitly assumed that the wavefunction exist (unit norm) on a large enough grid and that after a time $t > t_f$ ($= T/\beta$ in our case), there are no time dependent interactions: $H = H_0$. Our wavefunction is then, at $t = t_f$

$$\Psi(r_i, \theta_j, t_f) = \sum_{l=0}^{L_{max}} f_l(r_i, t_f) e^{i\mathbf{p}\cdot\mathbf{r}} Y_{l,0}(\theta_j). \tag{3}$$

Note that this is the 'reduced' wavefunction, see [**?**]. All radial functions have been multiplied with r such that the normalization is simply,

$$1 = \sum_{l=0}^{L_{max}} \int_0^{r_{max}} dr |f_l(r)|^2 \tag{4}$$

Division with 'r' or needs to be taken into account when equating the numerical wavefunction with Eq. (1). To extract differential quantities one need (and we may in fact always do it like this) to project onto the basis of Coulomb functions existing on the very same grid. From the solution of the Coulomb problem we extract a discrete set of basis functions which are zero at the end of the grid.

But let us first see what happens when we project onto a plane wave basis $|\mathbf{p}\rangle$, with

$$\langle \mathbf{r}|\mathbf{p}\rangle = \frac{1}{(2\pi)^{3/2}} e^{i\mathbf{p}\cdot\mathbf{r}} \tag{5}$$

The calculation will involve using a well known expansion of the plane wave as,

$$e^{i\mathbf{p}\cdot\mathbf{r}} = 4\pi \sum_{L,M\in(-L,L)}^{\infty} i^L j_L(pr) Y^*_{L,M}(\hat{p}) Y_{L,M}(\hat{r}) \tag{6}$$

Here j_L is the spherical Bessel function, $j_l(x) = \frac{1}{\sqrt{x}} J_{l+0.5}(x)$.

Then,

$$\langle \mathbf{p}|\Psi\rangle = \sum_{l=0}^{L_{max}} (-i)^l \left[\sqrt{\frac{2}{\pi}}\int_0^\infty r f_l(r,t) j_l(pr) dr\right] Y_{l,0}(\hat{p}) \quad (7)$$

$$= \sum_{l=0}^{L_{max}} \tilde{f}_l(p) Y_{l,0}(\hat{p}) \quad (8)$$

since $\int d\hat{r} Y^*_{L,M}(\hat{r}) Y_{l,m}(\hat{r}) = \delta_{L,l}\delta_{M,m}$. **This is the full time-dependent wavefunction in momentum space.** Clearly, according to the interpretation of quantum mechanics, $|\sum_{l=0}^{L_{max}} p_i \tilde{f}_l(p_i) Y_{l,0}(\hat{p}_i)|^2 dp$ is the probability of the total wavefunction to have a momentum component p_i.

We shall be interested in momentum components belonging to outgoing waves, not all momentum components above which also include the contribution from bound states. By expressing the numerical radial wavefunction as a bound part and a continuum part, $f_l(r,t_f) = f_l^b(r,t_f) + f_l^c(r,t_f)$ it is straight forward to replace $f_l(r,t)$ by $f_l^c(r,t_f)$ in the equation above and we obtain,

$$\langle \mathbf{p}|\Psi^c\rangle = \sum_{l=0}^{L_{max}} \left[\sqrt{\frac{2}{\pi}}\int_0^\infty r f_l^c(r,t) j_l(pr) dr\right] Y_{l,0}(\hat{p}) \quad (9)$$

$$= \sum_{l=0}^{L_{max}} \tilde{f}_l^c(p) Y_{l,0}(\hat{p}) \quad (10)$$

The differential cross section per (scalar) momentum becomes Eq. (9) of the manuscript.

$$\frac{d\sigma}{dp_n} = \int d\hat{p} p^2 |\langle \mathbf{p}|\Psi(\mathbf{r},t_f)\rangle|^2 = \sum_{l=0}^{L_{max}} |p_n \tilde{f}_l^c(p_n,t_f)|^2 \quad (11)$$

The differential angular resolved cross section can hardly be obtained in this way. That is because the momentum states are not the correct basis of the Coulomb problem. One way to understand this is to consider an alternative basis expansion in terms of the bound states and the discrete continuum states which vanish at $r = r_{max}$,

$$\Psi(\mathbf{r},t_f) = \sum_m a_m(t_f)\Phi_m(\mathbf{r}) + \sum_n b_n(t_f)\Phi_n^c(\mathbf{r}) \quad (12)$$

The second sum is the discretized representation of the continuum, $\Phi_n^c(\mathbf{r}) = \phi_{n,l}^c(r;p_n) Y_{l,0}(\hat{r})$ Now, the projection onto momentum states becomes

$$\langle \mathbf{p}|\Psi\rangle = \sum_{l=0}^{L_{max}} \sum_n (-i)^l \left[\sqrt{\frac{2}{\pi}}\int_0^\infty r^2 j_l(pr)\phi_n^c(r,p_n) dr\right] b_n(t_f) Y_{l,0}(\hat{p}) \quad (13)$$

The term in the parenthesis is an overlap, in general nonzero for any p, which makes it very troublesome to compute. In addition, one needs the set of functions $\phi_n^c(r,p_n)$ on pre-calculated form. This is the basis defined by being radial solutions of H_0 with positive energy and vanishing at r_{max}. Therefore, when angular quantities which will be considered it would be good if we instead could calculate them directly from the numerical basis at hand, in radial ($f_l^c(r)$) or momentum space ($\tilde{f}_l^c(p)$).

In text books, it is shown that the solution of the Coulomb problem in terms of outgoing regular basis functions (vanishing at $r \to 0$) can be written in atomic units, $p = k$, $E = p^2/2$,

$$\Psi_C(\mathbf{r}) = 4\pi \sum_{l=0}^{\infty} \sum_n (i)^l e^{i\delta_l} \frac{F_l(\eta; rp)}{pr} Y^*_{l,0}(\hat{p}) Y_{l,0}(\hat{r}) \tag{14}$$

where $\eta = 1/p$ for hydrogen, the Coulomb phase shift is $\delta_l(p_i) = \arg[\Gamma(l+1-i/p_i)]$ and F_l is the solution to the reduced radial Schrödinger equation with the Coulomb potential and has the asymptotic behaviour,

$$F_l \underbrace{\sim}_{r\to\infty} \sin(pr - \frac{1}{2}l\pi - \eta \ln(2pr) + \delta_l) \tag{15}$$

By comparing, the relation between the continuum basis functions of Eq. (12) and Eq. (15), becomes,

$$\phi^c_{n,l}(r; p_n) = \frac{F_l(\eta; rp_n)}{4\pi r} \tag{16}$$

The expansion in a basis with the correct asymptotic phases is therefore

$$\Psi_C(\mathbf{r}) = \sum_{l=0}^{\infty} \sum_n (i)^l e^{i\delta_l} \phi^c_{n,l}(r; p_n) Y^*_{l,0}(\hat{p}) Y_{l,0}(\hat{r}) \tag{17}$$

This makes projection onto these states particularly simple:

$$\langle \Psi_C(\mathbf{r}) | \Psi(\mathbf{r}, t_f) \rangle = \frac{1}{p} \sum_{l=0}^{L_{max}} \sum_n (-i)^l e^{-i\delta_l} b_n(t_f) Y_{l,0}(\hat{p}) \tag{18}$$

The differential cross section per momentum again becomes,

$$\frac{d\sigma}{dp_n} = \int d\hat{p} p_n^2 |\langle \Psi_C(\mathbf{r}) | \Psi(\mathbf{r}, t_f) \rangle|^2 = \sum_{l=0}^{L_{max}} |b_n(t_f)|^2 \tag{19}$$

The sum over l for fixed n means to take the sum of probabilities for fixed momentum (or energy). The differential angular cross section becomes,

$$\frac{d\sigma}{d\hat{p}} = \int dp p^2 |\langle \Psi_C(\mathbf{r}) | \Psi(\mathbf{r}, t_f) \rangle|^2 = \sum_n |\sum_{l=0}^{L_{max}} (-i)^l e^{-i\delta_l} b_n(t_f) Y_{l,0}(\hat{p})|^2 \tag{20}$$

cf. Eq. (9) of [54].

The formulae becomes equally simple for a grid expansion since, $b_n(t_f) = \langle \phi^c_{n,l}(r; p_n) | f^c_l(r,t) \rangle$

$$\begin{aligned} \langle \Psi_C(\mathbf{r}) | \Psi(\mathbf{r}, t_f) \rangle &= \sum_{l=0}^{L_{max}} \sum_n (-i)^l e^{-i\delta_l} \langle \phi_n | f_l \rangle Y_{l,0}(\hat{p}) & (21) \\ &= \sum_{l=0}^{L_{max}} (-i)^l e^{-i\delta_l} \tilde{f}^c_l(p, t_f) Y_{l,0}(\hat{p}) & (22) \end{aligned}$$

The last equation is valid precisely because the sum of projections is exactly equal to the Fourier transform of the continuum part of $f_l(r, t_f)$:

$$\sum_n \langle \phi_n | f_l \rangle = \sum_n \langle \phi_n | f^c_l \rangle = \sum_n \int dp \langle \phi_n | p \rangle \langle p | f^c_l \rangle = \tilde{f}^c_l(p) \tag{23}$$

The differential cross sections now becomes,

$$\frac{d\sigma}{dp_n} = \int d\hat{p} p_n^2 |\langle \Psi_C(\mathbf{r}) | \Psi(\mathbf{r}, t_f) \rangle|^2 = \sum_{l=0}^{L_{max}} |p_n \tilde{f}_l^c(p_n, t_f)|^2 \tag{24}$$

and

$$\frac{d\sigma}{dp_n d\hat{p}} = p_n^2 |\langle \Psi_C(\mathbf{r}) | \Psi(\mathbf{r}, t_f) \rangle|^2 = |\sum_{l=0}^{L_{max}} (-i)^l e^{-i\delta_l} p_n \tilde{f}_l^c(p_n, t_f) Y_{l,0}(\hat{p})|^2 \tag{25}$$

Observe that Eq. (11) and Eq. (24) are completely identical. This has to do with the definition of f_l^c: Having subtracted the "bound part" it is implicitly expressed in a basis of positive energy scattering states. However, for left-right (or forward-backward) scattering we have to use Eq. (25) and sum over angles, $\theta \in (0, \pi/2)$ for forward scattering, $\theta \in (\pi/2, \pi)$ for backward scattering. The additional phases in the last equation and their consequences are the origin of the new figure.

Graphic design: Communication Division, UiB / Print: Skipnes Kommunikasjon AS

uib.no

ISBN: 978-82-308-3704-7